

The origin of the diverse morphologies and kinematics of Milky Way-mass galaxies in the FIRE-2 simulations

Shea Garrison-Kimmel ¹★†, Philip F. Hopkins ¹, Andrew Wetzel ^{1,2,3}‡, Kareem El-Badry ⁴, Robyn E. Sanderson ^{1,5}, James S. Bullock ⁶, Xiangcheng Ma ¹, Freeke van de Voort ^{7,8}, Zachary Hafen ⁹, Claude-André Faucher-Giguère ⁹, Christopher C. Hayward ¹⁰, Eliot Quataert ⁴, Dušan Kereš ¹¹ and Michael Boylan-Kolchin ¹²

¹TAPIR, California Institute of Technology, Mailcode 350-17, Pasadena, CA 91125, USA

²The Observatories of the Carnegie Institution for Science, Pasadena, CA 91101, USA

³Department of Physics, University of California, Davis, CA 95616, USA

⁴Department of Astronomy and Theoretical Astrophysics Center, University of California Berkeley, Berkeley, CA 94720, USA

⁵Department of Astronomy, Columbia University, 550 W 120th St, Mail Code 5246, New York, NY 10027, USA

⁶Center for Cosmology, Department of Physics and Astronomy, University of California, Irvine, CA 92697, USA

⁷Heidelberg Institute for Theoretical Studies, Schloss-Wolfsbrunnengasse 35, D-69118, Heidelberg, Germany

⁸Astronomy Department, Yale University, PO Box 208101, New Haven, CT 06520-8101, USA

⁹Department of Physics and Astronomy and CIERA, Northwestern University, 2145 Sheridan Road, Evanston, IL 60208, USA

¹⁰Center for Computational Astrophysics, Flatiron Institute, 162 Fifth Avenue, New York, NY 10010, USA

¹¹Department of Physics, Center for Astrophysics and Space Science, University of California at San Diego, 9500 Gilman Drive, La Jolla, CA 92093, USA

¹²Department of Astronomy, The University of Texas at Austin, 2515 Speedway, Stop C1400, Austin, TX 78712, USA

Accepted 2018 September 10. Received 2018 August 13; in original form 2017 December 11

ABSTRACT

We use hydrodynamic cosmological zoom-in simulations from the Feedback in Realistic Environments project to explore the morphologies and kinematics of 15 Milky Way (MW)-mass galaxies. Our sample ranges from compact, bulge-dominated systems with 90 per cent of their stellar mass within 2.5 kpc to well-ordered discs that reach $\gtrsim 15$ kpc. The gas in our galaxies always forms a thin, rotation-supported disc at $z = 0$, with sizes primarily determined by the gas mass. For stars, we quantify kinematics and morphology both via the fraction of stars on disc-like orbits and with the radial extent of the stellar disc. In this mass range, stellar morphology and kinematics are poorly correlated with the properties of the halo available from dark matter-only simulations (halo merger history, spin, or formation time). They more strongly correlate with the gaseous histories of the galaxies: those that maintain a high gas mass in the disc after $z \sim 1$ develop well-ordered stellar discs. The best predictor of morphology we identify is the spin of the gas in the halo at the time the galaxy formed 1/2 of its stars (i.e. the gas that builds the galaxy). High- z mergers, before a hot halo emerges, produce some of the most massive bulges in the sample (from compact discs in gas-rich mergers), while later-forming bulges typically originate from internal processes, as satellites are stripped of gas before the galaxies merge. Moreover, most stars in $z = 0$ MW-mass galaxies (even $z = 0$ bulge stars) form in a disc: $\gtrsim 60$ –90 per cent of stars begin their lives rotationally supported.

Key words: galaxies: bulges – galaxies: evolution – galaxies: formation – galaxies: spiral – galaxies: structure – cosmology: theory.

1 INTRODUCTION

Galactic morphologies vary widely. Broadly speaking, galaxies range from elliptical, dispersion-supported systems to disc-dominated structures where the majority of stars are on well-ordered

* E-mail: sheagk@caltech.edu

† Einstein Fellow.

‡ Caltech-Carnegie Fellow.

circular orbits (e.g. Hubble 1926; Huertas-Company et al. 2011). The former dominate at both the high-mass end (e.g. Bamford et al. 2009) and at the low-mass end (e.g. Wheeler et al. 2017), with discy galaxies emerging primarily at intermediate stellar masses of $\sim 10^9$ – $10^{11} M_{\odot}$ (e.g. Simons et al. 2015). The preponderance of ellipticals at the high-mass end is typically associated with these galaxies growing primarily through dry mergers (van Dokkum 2005; van Dokkum et al. 2010; Rodríguez-Puebla et al. 2017), which scramble stellar orbits and promote bulge formation (e.g. White & Rees 1978; Hopkins et al. 2009a; Stewart et al. 2009; Hopkins et al. 2010). At the low-mass end, stars are both born out of gas with a high degree of pressure support (rather than rotational support), and they are then dynamically heated by the repeated cycles of gas blowouts that continue to $z \sim 0$ in $\lesssim 10^{11} M_{\odot}$ haloes (e.g. Kaufmann, Wheeler & Bullock 2007; Pontzen & Governato 2012; El-Badry et al. 2016, 2018; Faucher-Giguère 2018).

At intermediate masses, however, the exact properties of a galaxy and/or halo that drive the morphology of that system remain relatively poorly understood. Mo, Mao & White (1998, hereafter M98) reproduced both the $z = 0$ population of disc galaxies and the properties of $z \sim 2.5$ damped Ly α systems in semi-analytic models by using a slightly modified form¹ of a model introduced in Fall (1983, hereafter F83) that assumed (1) galaxy sizes are determined by their angular momentum, (2) the baryons in a galaxy acquire their angular momentum from the host dark matter (DM) halo, (3) DM haloes respond adiabatically to the growth of galaxies, and (4) baryons initially have the same density profile as DM (also see Fall & Efstathiou 1980; Romanowsky & Fall 2012; Fall & Romanowsky 2013). This model therefore predicts that the size of a galactic disc (relative to the radius of the halo) depends primarily on the spin of the host DM halo, such that elliptical galaxies reside in low angular momentum haloes.

Though the Fall (1983) paradigm broadly reproduces the galactic population, it has not been possible to directly test it against hydrodynamic simulations that include star formation and feedback, the latter of which appears to be particularly important for regulating the angular momentum (and therefore shapes) of galaxies. Such simulations typically fall into two categories: large-volume simulations such as Illustris (Vogelsberger et al. 2014a,b), IllustrisTNG (Weinberger et al. 2017; Pillepich et al. 2018), and EAGLE (Evolution and Assembly of GaLaxies and their Environments; Schaye et al. 2015); and ‘zoom-in’ simulations (Katz & White 1993; Oñorbe et al. 2014) that focus on individual systems. While the former contain huge populations of galaxies in a given mass bin ($\gg 10^3$), each galaxy typically contains $\lesssim 10^3$ resolution elements, with spatial resolutions $\gtrsim 1$ kpc, such that it is impossible to fully resolve the vertical scale lengths of Milky Way (MW)-like discs. However, recent work with this style of simulations have managed to broadly reproduce the observed Hubble sequence of galaxy types (e.g. Pedrosa, Tissera & De Rossi 2014; Pedrosa & Tissera 2015; Genel et al. 2015; Teklu et al. 2015; Zavala et al. 2016; Genel et al. 2018). In particular, Rodríguez-Gomez et al. (2017) found that the morphologies of massive systems ($M_{\text{galaxy}}^* \geq 10^{11} M_{\odot}$) in the Illustris simulation are determined by their merger histories, while the morphologies of low-mass galaxies ($M_{\text{galaxy}}^* \leq 10^{10} M_{\odot}$) correlate with their host halo spin. However, they found that neither spin nor merger history could individually explain morphologies at the

intermediate-mass scale occupied by the MW. Zavala et al. (2016), meanwhile, used the EAGLE simulation to show a co-evolution between the specific angular momentum of the stars in a galaxy today, which is related to the morphology of that galaxy, and that of the inner DM halo where the galaxy resides.

Conversely, zoom-in simulations excel at resolving the structure of the galaxy (or galaxies) that they target, but each additional galaxy incurs a significant CPU cost, such that many suites of zoom-in simulations only include a few galaxies at a given mass simulated with a given physical model. There are thus only a few suites of hydrodynamic zoom-in runs (e.g. GIMIC, Crain et al. 2009; MAGICC, Stinson et al. 2012; NIHAO, Wang et al. 2015; Auriga, Grand et al. 2017) that have the sample size to test and explore even basic correlations between morphology and halo properties (such as the Fall 1983 model). However, some trends have emerged across a number of analyses of various zoom-in simulations, which have generally become successful in recent years at producing realistic disc galaxies (Governato et al. 2007, 2009; Scannapieco et al. 2009; Guedes et al. 2011; Aumer et al. 2013; Marinacci, Pakmor & Springel 2014; Fiacconi, Feldmann & Mayer 2015; Murante et al. 2015; Colín et al. 2016). A wide variety of authors using different simulation codes agree that stellar feedback is crucial for regulating star formation in low angular momentum material, which otherwise quickly collapses to form overly massive bulge components (Okamoto et al. 2005; Scannapieco et al. 2008; Agertz, Teyssier & Moore 2011; Roškar et al. 2014; Agertz & Kravtsov 2016; Brooks & Christensen 2016).

Some of these authors have examined the conditions that lead to disc formation. For example, Springel & Hernquist (2005) and Robertson et al. (2006) found that mergers of gas-rich galaxies can result in an extended star-forming disc, rather than a bulge-dominated system (also see Robertson & Bullock 2008). Similarly, Governato et al. (2007) found that a substantial disc formed following a gas-rich major merger in a cosmological simulation. Governato et al. (2009) also examined the distribution of *light* at $z = 0$ in a galaxy that experienced a major merger at $z = 0.8$, and found that this violent merger primarily grows the disc, rather the bulge. Combined with the passive evolution of the older stars in the bulge, this fresh star formation results in a bright, blue stellar disc. Together, these results suggest that gas-rich major mergers can lead to extended stellar discs (Hopkins et al. 2009b), particularly if they occur at late times when the potential is deep enough to prevent the burst-quench cycles that occur at higher redshift (Muratov et al. 2015; Sparre et al. 2017; Faucher-Giguère 2018), which heat stellar orbits and generally inhibit disc formation.

Other works have used suites (of varying sizes) of zoom-in simulations to attempt to uncover the underlying drivers of stellar morphology. Scannapieco et al. (2009), for example, argued that the fraction of mass in the disc does not depend on the spin parameter of the halo, but instead that the individual formation history of each galaxy is crucial to predicting its $z = 0$ morphology. They also showed that spheroidal (bulge) components typically form earlier, while discs tend to form at later times from the inside-out (also see Aumer et al. 2013; Sokołowska et al. 2017), in general agreement with observations tracing the evolution of the kinematics of gas in galaxies (Simons et al. 2017). Using a set of 100 MW-mass haloes in high-resolution regions embedded within the Millennium (Springel et al. 2005) simulation volume, Sales et al. (2012) similarly found that galaxy morphology was not correlated with the spin of the halo. They then further showed that it also does not monotonically depend on either the halo formation time (which scales with the concentration of a halo; e.g. Ludlow et al. 2014) or the merger

¹Mo et al. (1998) applied the Fall (1983) formalism to an initially NFW (Navarro, Frenk & White 1996) profile, rather than the isothermal profile assumed by Fall (1983).

history: even haloes that grow significantly through major mergers can host either a disc-dominated or a bulge-dominated system at $z = 0$. Instead, they argued that the star formation history is key: discs tend to form gradually and at late times, while spheroidal components assemble in episodic bursts of star formation that occur following the accretion of gas that is misaligned from the existing galaxy. More recently, Grand et al. (2017) used 30 galaxies from the Auriga Project to argue (1) that disc size *does* correlate with halo spin (though the kinematic disc fraction, which we define below, does not) and (2) that well-aligned mergers of gas-rich satellites promote disc growth.

Collectively, the results from large-volume and zoom-in simulations suggest that a picture where stellar morphology is regulated by angular momentum is not necessarily wrong, but that it is likely incomplete. However, the majority of these studies have focused on simulations that adopt a stiff equation of state for the interstellar medium, which could plausibly introduce artefacts into, e.g. the behaviour of the gas during galactic mergers, motivating a study with a more physical description of the interstellar medium. Here, we use a sample of 15 MW-mass galaxies, seven of which are isolated and eight of which are in Local Group-like pairs, from high-resolution zoom-in simulations, run with physically motivated and identical models and parameters for star formation and feedback, to explore correlations and drivers of (primarily) stellar morphology. We first test the Fall (1983) predictions against the sizes of our galaxies, then search for physically meaningful correlations between stellar morphology at $z = 0$ and various properties of the host halo, including their evolutionary histories. We then explore the evolution of the stellar morphologies and the fraction of stars born in a disc at any given time to better understand the impact of dynamical interactions and the instantaneous state of the star-forming gas at any given time. Finally, we examine the morphology of the gas at $z = 0$ to understand the morphologies of stars being born today.

Throughout this work, we assume flat Λ cold dark matter cosmologies, with $h = 0.68\text{--}0.71$, $\Omega_m = 0.266\text{--}0.31$, $\Omega_b = 0.0455\text{--}0.048$, and $\Omega_\Lambda = 1 - \Omega_m$ (e.g. Larson et al. 2011; Planck Collaboration et al. 2016).² We adopt the Bryan & Norman (1998) definition of M_{vir} and R_{vir} throughout, except when computing the Fall (1983) predictions, which depend on the properties of the halo within R_{200} , the radius at which the density is 200 times the critical density. For all stellar images and properties presented herein, we use a coordinate system where the z -axis is aligned with the shortest principal axis of the moment of inertia tensor of all star particles within 20 kpc. For the gas, we align our coordinate system with the shortest principal axis of the gas within 10 kpc; we select a smaller radius for the gas because the gas moment of inertia tensor at 20 kpc is occasionally dominated by gas outside the galaxy. We sometimes refer to halo properties in the corresponding DM-only simulation; such properties will be indicated as ‘DMO’.

We explicitly opt not to make comparisons with observations in this work because our goal is not to demonstrate the ‘reasonableness’ of our galactic discs, but rather to understand why and how they came to have their $z = 0$ morphologies. However, we note that the Feedback in Realistic Environments (FIRE)/FIRE-2 physics are broadly successful at reproducing observed galactic properties over

a range of galaxy masses, including the stellar mass *versus* halo mass relation (Hopkins et al. 2014, 2018), the normalization and scatter of the star formation rate (SFR) *versus* stellar mass relationship (Sparre et al. 2017), the Kennicutt–Schmidt law (Orr et al. 2018), the mass–metallicity relationship (Ma et al. 2016), and even the vertical and radial structure (including stellar ages and metallicities) of the MW disc (Ma et al. 2017b). Sanderson et al. (2017) also show that the masses of the stellar haloes around the FIRE-2 MW-mass galaxies are in relative agreement with those measured by Merritt et al. (2016). Moreover, proper comparisons to observations requires a careful conversion from the stellar mass to observed light to make a fair comparison with observables, including the effects of dust attenuation and stellar evolution (e.g. radial variations in the mass-to-light ratio; Wuyts et al. 2010). Scannapieco et al. (2010), for example, used mock observations to show that photometric bulge/disc decompositions typically overestimate the true disc fractions by at least a factor of two. A detailed comparison of observer-space disc indicators will be the focus of subsequent work(s).

This paper is organized as follows. In Section 2, we describe the simulations and briefly review the star formation and feedback models. Section 3 presents our measures of morphology, f_{disc}^* and R_{90}^* , and compares them to other (primarily theoretical) quantifiers. Section 4 compares the actual morphologies to those predicted by the Fall (1983) and Mo et al. (1998) models, then presents correlations between $z = 0$ morphologies and various properties of the galaxy and their host haloes, while Section 5 explores the evolution of the stellar morphologies and the birth properties of stars. Section 6 presents the morphologies of the gas discs in our sample. We summarize our results and conclusions in Section 7.

2 SIMULATIONS

We analyse hydrodynamic, cosmological zoom-in (Katz & White 1993; Oñorbe et al. 2014) simulations from the FIRE³ project, specifically with the improved ‘FIRE-2’ version of the code from Hopkins et al. (2018). In order to maximize our sample size, we include simulations with varying resolutions, which we discuss below, but the numerical methods and primary physical models are identical across all of the simulations. All of the simulations were run using GIZMO (Hopkins 2015),⁴ a multimethod gravity plus hydrodynamics code, in meshless finite-mass (‘MFM’) mode. This is a mesh-free Lagrangian finite-volume Godunov method which automatically provides adaptive spatial resolution while maintaining conservation of mass, energy, and momentum (for extensive tests, see Hopkins 2015). Gravity is solved with an improved version of the TREEPM solver from GADGET-3 (Springel 2005), with fully adaptive (and fully conservative) gravitational force softening for gas (so hydrodynamic and force softening are always self-consistently matched), following Price & Monaghan (2007).

The FIRE physics and source code are *exactly* identical to those in previous FIRE-2 simulations; these are described in detail in the papers above but we briefly review them here. Radiative heating and cooling is treated (from 10 to 10^{10} K), including free–free, photoionization/recombination, Compton, photoelectric, and dust collisional, cosmic ray, molecular, and metal-line and fine-structure processes (following each of 11 tracked species independently), and accounting for photoheating both by an ultraviolet (UV) background

²The differences in average halo properties due to variances in the cosmological parameters are smaller than the typical halo-to-halo variance within a given cosmology, and, moreover, any systematic variations would be automatically included in the physical parameters we explore here.

³<http://fire.northwestern.edu>

⁴<http://www.tapir.caltech.edu/~phopkins/Site/GIZMO.html>

Table 1. Properties of the central galaxies and their host haloes, sorted by decreasing f_{disc}^* . In order, columns indicate the host halo virial mass, the stellar and gas mass of the central galaxy (defined in Section 3.2), the fraction of stars in the central galaxy on ‘disc-like’ orbits ($\varepsilon \geq 0.5$), and the sizes of the stellar and gas discs (see Section 3.1 for details). To give an estimate of how sensitive the disc fractions/ordering are to our $\varepsilon \geq 0.5$ cut, the following column lists the fraction of stellar mass with $\varepsilon \geq 0.7$. The remaining columns list the resolution of each simulation, given by the initial gas particle mass and the mass of the DM particles in the high-resolution region. We refer the reader to Hopkins et al. (2018) for an in-depth discussion of the spatial resolutions of the simulations, and their meanings, but we note here that the mean interparticle spacing in star-forming gas (which is directly tied to the adaptively varying gravitational/hydrodynamic smoothing length) is typically 7–13pc, while the gravitational smoothing lengths of the stars and DM are fixed at approximately the mean interparticle spacing expected at the centre of the halo. The final column lists the publication each run first appeared in: A: Hopkins et al. (2018), B: Garrison-Kimmel et al. (2017), C: Wetzel et al. (2016), D: Hafen et al. (2017), E: this work. Galaxies beginning with ‘m12’ are isolated MW-mass analogues, while those with names of individuals are in Local Group-like pairs. Romulus & Remus and Thelma & Louise are hydrodynamic re-simulations of the same pairs originally presented (as DMO simulations) in Garrison-Kimmel et al. (2014). Figs 5 and 14 plot the relationships between several of these properties.

Galaxy	M_{vir} [$10^{12} M_{\odot}$]	M_{galaxy}^* [$10^{10} M_{\odot}$]	$M_{\text{galaxy}}^{\text{gas}}$ [$10^{10} M_{\odot}$]	f_{disc}^*	R_{90}^* [kpc]	Z_{90}^* [kpc]	R_{gas} [kpc]	$f_{\geq 0.7}^*$	$m_i, \text{ gas}$ [$10^3 M_{\odot}$]	m_{DM} [$10^4 M_{\odot}$]	Reference
Romeo	1.28	6.98	3.78	0.79	17.4	1.95	30.5	0.65	28	15	A
Juliet	1.06	5.26	2.49	0.76	13.7	1.67	20.8	0.59	28	15	A
Louise	1.10	6.39	3.15	0.69	12.2	1.5	24.2	0.56	32	16	A
Robin	1.56	5.99	2.65	0.66	9.5	1.65	20.8	0.51	57	31	A
Thelma	1.44	11.58	1.64	0.65	11.6	2.13	11.2	0.5	32	16	A
m12f	1.58	7.53	2.18	0.64	11.1	2.39	20.8	0.48	7.1	3.5	B
Romulus	1.95	13.46	3.63	0.61	11.6	2.55	22.4	0.48	32	16	E
m12i	1.14	6.16	1.81	0.58	9.9	2.07	17.8	0.44	7.1	3.5	C
m12z	0.86	3.5	1.07	0.57	11.4	3.23	8.3	0.4	33	17	D
m12c	1.27	8.09	0.25	0.56	4.3	1.08	3.6	0.42	57	28	A
Remus	1.23	10.05	0.71	0.53	7.7	1.71	8.3	0.45	32	16	E
m12m	1.47	10.88	1.01	0.53	13.3	2.75	12.1	0.34	7.1	3.5	A
m12b	1.36	9.13	1.4	0.33	5.2	1.16	12.1	0.27	57	28	A
m12q	1.61	11.23	0.12	0.21	5.4	1.57	0.9	0.11	57	28	A
Batman	1.89	10.21	0.93	0.20	2.4	0.98	11.2	0.08	57	31	A

(Faucher-Giguère et al. 2009) and an approximate model for local sources, and self-shielding. Star formation occurs only in gas identified as self-gravitating according to the Hopkins, Narayanan & Murray (2013) criterion, which is also molecular and self-shielding (following Krumholz & Gnedin 2011), Jeans unstable, and exceeds a minimum density threshold $n_{\text{min}} = 1000 \text{ cm}^{-3}$. Once a star particle forms, the simulations explicitly follow several different stellar feedback mechanisms, including (1) local and long-range momentum flux from radiation pressure (in the initial UV/optical single-scattering, and re-radiated light in the IR), (2) energy, momentum, mass, and metal injection from SNe (Types Ia and II) and stellar mass loss (both OB and asymptotic giant branch), and (3) photoionization and photoelectric heating. Every star particle is treated as a single stellar population with known mass, age, and metallicity, and then all feedback event rates, luminosities and energies, mass-loss rates, and all other quantities are tabulated directly from stellar evolution models (STARBURST99; Leitherer et al. 1999), assuming a Kroupa (2001) initial mass function. We emphasize that the FIRE physics were not tuned to reproduce galaxy sizes or morphologies. One of the pairs, Romulus & Remus, was simulated with subgrid turbulent metal diffusion (Hopkins 2017; Escala et al. 2018); however, Su et al. (2017) showed metal diffusion has a small impact on the morphology of an MW-mass galaxy.

We focus on the roughly MW-mass galaxies simulated with FIRE-2. Therefore, we combine the Latte halo (here referred to as m12i) from Wetzel et al. (2016); five additional isolated haloes simulated with an identical pipeline, two at the same resolution and three with a factor of eight higher mass particles; one isolated halo from Hafen et al. (2017), three pairs of haloes in Local Group-like configurations (first reported in Hopkins et al. 2018, but analysed in detail here for the first time), and one additional pair that has not yet been reported elsewhere. Hosts in Local Group-like pairs were selected with the same criteria as Garrison-Kimmel et al. (2014):

isolated pairs with $M_{\text{vir}} \sim 10^{12} M_{\odot}$ that are approaching one another. All other hosts were selected purely on the basis of their mass and isolation from other massive haloes. The mass resolution of each galaxy is listed in Table 1.⁵ Softening lengths for the gas are fully adaptive, typically down to 1pc, with fixed stellar and DM softening lengths set according to the typical interparticle spacing. Hopkins et al. (2018) list the exact values for our runs, but all are sufficient to resolve the disc heights. For each galaxy, we analyse the highest resolution simulation available that has been completed to $z = 0$. We demonstrate the stability of our morphologies and sizes with numerical resolution in Appendix A: the general trends are robust to resolution, but we caution that quantitative values do change slightly with resolution.

Movies showing the formation and evolution of each galaxy in our sample, created using identical pipelines, may be found at <http://www.tapir.caltech.edu/~sheagk/firemovies.html>.

3 QUANTIFYING MORPHOLOGY OF THE FIRE-2 GALAXIES

There are a wide variety of reasonable definitions for galactic morphology that one can adopt. Broadly speaking, they range from kinematic distinctions (e.g. the fraction of stars on circular orbits) to visual quantifiers (e.g. photometric bulge-to-disc ratios, Sérsic 1963 indices, and half-light radii). Though the former are straightforward to measure in simulations, they are difficult to determine with observations. The latter, however, are relatively straightforward to extract with photometry, but can only be measured for simulated

⁵We list the initial mass of a gas particle in each simulation, but note that due to deposition onto gas particles from stellar mass loss, baryonic particle masses fluctuate slightly about their initial value.

galaxies if one assumes models for stellar evolution and dust attenuation. Though the relationship between observable morphological measures and kinematic quantifiers is extremely interesting, a full study requires ‘mock observations’ of the simulated galaxies (including radiative transfer) and subsequent fitting of those images with the tools typically used by observers. We consider these steps to be beyond the scope of this paper, which instead focuses on the physical drivers of those morphologies, but plan to investigate this question in greater detail in future work.

3.1 Definitions

Here, we focus primarily on morphological measures that do not rely on specific profiles or on assumptions regarding the luminosities/colours of individual star particles. We primarily adopt two independent measures of galactic morphology, f_{disc}^* and R_{90}^* . The latter, R_{90}^* , is the radial extent of the disc. It is defined together with Z_{90}^* , the height of each galaxy, such that 90 per cent of the stellar mass within 30 kpc of the galactic centre is contained within a 2D radius R_{90}^* and a height above/below the disc Z_{90}^* when the stars are aligned with their principal axes. We then define M_{galaxy}^* as the stellar mass within a radial distance R_{90}^* and a height above/below the disc Z_{90}^* .⁶ For the purposes of comparing with semi-analytic models (Section 4.2), we identically define R_{50}^* , the 2D radius that encloses 50 per cent of the stellar mass. We similarly define 3D stellar radii $r_{90,3\text{D}}^*$ and $r_{50,3\text{D}}^*$ as the radii that contain 90 per cent and 50 per cent of the stellar mass within 30 kpc. Though the same process typically yields accurate results for the gas, it artificially inflates the sizes of extremely gas-poor galaxies (e.g. m12c and m12q; see Fig. 13). Therefore, we define the radial and vertical extents of the gas disc by first taking the peak of the face-on mass profile, $dM_{\text{gas}}(R)/d\ln R$, as R_{gas} , then defining Z_{gas} as the break in the vertical 1D mass profile of all the gas with a projected radius $R < R_{\text{gas}}$. $M_{\text{galaxy}}^{\text{gas}}$ is then defined as the total gas mass within $(R_{\text{gas}}, Z_{\text{gas}})$. $M_{\text{galaxy}}^{\text{gas}}$ typically changes by only ~ 10 – 20 per cent between this method and the approach we adopt for the stars, with the technique we adopt for the gas yielding a slightly lower $M_{\text{galaxy}}^{\text{gas}}$ in all but two cases.⁷ All properties are based on centres calculated via a shrinking spheres approach (Power et al. 2003).

Our kinematic morphological definition, f_{disc}^* , measures the fraction of stars on circular orbits that are aligned with the angular momentum of all of the stars in the galaxy.⁸ Specifically, for each particle within $r_{90,3\text{D}}^*$, we compute the circularity $\varepsilon = j_z/j_{\text{circ}}(E)$ following the method of Abadi et al. (2003) and described in detail in El-Badry et al. (2018). For a given mass element, the circularity relates the component of the specific angular momentum that is aligned with the average angular momentum vector of the galaxy, j_z , to the specific angular momentum of a circular orbit with the same energy, $j_{\text{circ}}(E)$. Stars (or gas) with $\varepsilon = 1$ are therefore on perfectly circular orbits in the plane of the galaxy, those with $\varepsilon = 0$ have orbits that are exactly perpendicular to the galaxy, and those with $\varepsilon = -1$ are perfectly counter-rotating. We adopt a cut of $\varepsilon \geq 0.5$ to distinguish disc stars, and define f_{disc}^* as the mass fraction of stars that meet this cut within $r_{90,3\text{D}}^*$. We find nearly identical

disc fractions if we consider all stars within 30 kpc: the fractional difference is typically < 5 per cent.

3.2 Simulation properties

The distributions of ε for both the stars and gas in each MW-mass FIRE-2 galaxy (i.e. within $r_{90,3\text{D}}^*$) are shown in Fig. 1. Each panel represents an individual galaxy; they are ordered by decreasing f_{disc}^* , which is indicated for each galaxy. The number in parentheses below f_{disc}^* indicates the rank that each galaxy *would* have if they were instead ordered by decreasing R_{90}^* ; we compare f_{disc}^* and R_{90}^* explicitly in Fig. 3. We will retain this sorting by f_{disc}^* in other figures to ease comparison.

The stellar distributions, which are plotted as the coloured histograms in Fig. 1, vary widely even in our relatively small sample. Without pre-selecting for expected morphology, the MW-mass FIRE-2 sample includes nearly bulgeless disc galaxies (e.g. Romeo and Juliet), galaxies with clear bulge and disc components (e.g. Remus and m12b), and almost entirely dispersion-supported galaxies (Batman and m12q).⁹ The colour of each curve at a given ε indicates the average formation time of stars with that ε . Other than Batman and m12q, which have formed roughly counter-rotating discs at late times, the disc ($\varepsilon \geq 0.5$) is almost always composed of younger stars on average, in agreement with previous results that discs in MW-mass galaxies begin to appear at $z \lesssim 1$ (e.g. Ma et al. 2017b,a). In some cases, such as m12b and Remus, the average ages of the bulge and disc components differ dramatically, while the transition is much smoother in other systems (e.g. m12m and m12z).

In contrast with the diversity in the kinematics of the stars, the gas distributions (green dashed curves) are almost uniform across this mass-selected sample. Specifically, every galaxy except m12q (which has not experienced any significant gas accretion since $z \sim 0.1$) hosts a thin, primarily rotation-supported gas disc. The grey curves in Fig. 1, which show the circularity distributions of the stars formed in the galaxy *at birth* (i.e. stacking over all snapshots) are similarly uniform, with the vast majority of stars forming with $|\varepsilon| \geq 0.5$. We will discuss the kinematics of stars at birth along with the evolution of those kinematics in Section 5, and we will explore the characteristics of the gas discs in greater detail in Section 6, but we first focus on the $z = 0$ stellar morphologies.

Visualizations of the stars in all 15 galaxies are shown in Fig. 2, again sorted by f_{disc}^* . The top panels show face-on views of each galaxy, while the lower panels visualize the galaxy edge-on. There is a clear trend for galaxies to become more elliptical, less discy, and typically more spatially compact as f_{disc}^* decreases. The thick dashed and thin solid circles (rectangles) in the upper (lower) panels of Fig. 2 indicate (R_{90}^*, Z_{90}^*) and (R_{50}^*, Z_{50}^*) , respectively. As intended, the former captures roughly the full extent of the stellar populations. We also plot circular velocity profiles for the full sample in Appendix B: galaxies with higher disc fractions tend to have flatter, more extended circular velocity curves and, conversely, the bulge-dominated systems have rotation curves that peak at small radii, but there is some scatter about that trend.

We summarize several basic properties of each galaxy in Table 1, including the host virial mass M_{vir} , the galaxy stellar mass M_{galaxy}^* ,

⁶We note that this definition differs from the stellar masses listed in Hopkins et al. (2018), who quoted total stellar masses within $3 \times r_{50,3\text{D}}^*$.

⁷Nearly all of the gas (typically > 99 per cent) within $(R_{\text{gas}}, Z_{\text{gas}})$ has $T < 10^5$ K.

⁸We similarly define $f_{\text{gas}}^{\text{disc}}$, the fraction of gas on disc-like orbits, relative to all of the gas in the galaxy.

⁹We note that Batman and m12q are very compact, with $R_{50}^* \simeq 0.5$ and 1 kpc respectively, and may be outliers in observations (e.g. Shen et al. 2003). As noted, though, we caution against direct comparisons with observations without mock-observing the sample.

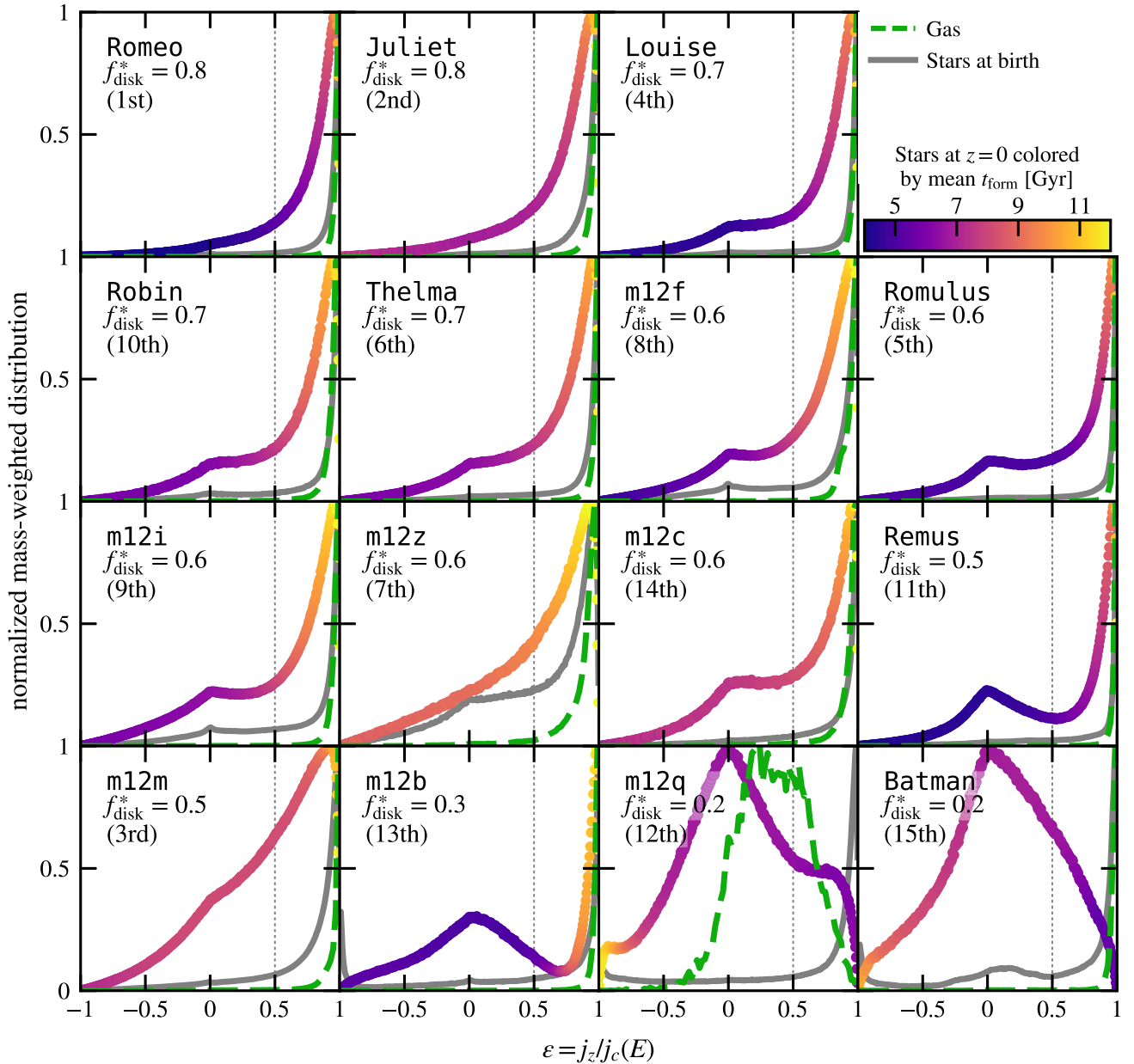


Figure 1. Mass-weighted distributions (normalized to a maximum of one) of the circularity $\varepsilon = j_z/j_c(E)$ for the stars (coloured histograms) and gas (dashed green curves) within the MW-mass FIRE-2 galaxies at $z = 0$. The stellar distributions are coloured by the average cosmic formation time (where $z = 0$ corresponds to $t_{\text{form}} \simeq 13\text{--}14$ Gyr) of the stars in each bin. The vast majority of the galaxies transition to younger ages at higher circularities; the exceptions are m12q and Batman, which form counter-rotating discs at late times. The grey curves show the kinematics measured when stars are born; we discuss them in detail in Section 5, but emphasize here that almost all stars are born in $z = 0$ MW-mass galaxies form on disc-like orbits (i.e. with very high circularities). We quantify the ‘disciness’ of a galaxy by f_{disc}^* , defined here as the fraction of stars with $\varepsilon \geq 0.5$, indicated by the dashed vertical line. The panels are sorted by decreasing f_{disc}^* , with the numbers in parentheses indicating the rank they would have if the panels were instead sorted from largest to smallest R_{90}^* , the 2D radial extent of the stars. We also demonstrate in Figs 3 and 4 that both f_{disc}^* and R_{90}^* correlate strongly with other kinematic and spatial measures of morphology. All but one of the galaxies has a well-ordered, rotating gas disc at $z = 0$; the exception is m12q, which is nearly gas-free and is in the process of expelling what little gas remains by $z = 0$. The stars display a range of kinematics ranging from well-ordered discs (Romeo) to dispersion supported bulges (Batman).

and the mass in gas within the galaxy $M_{\text{galaxy}}^{\text{gas}}$, along with the fraction of stars in the galaxy on circular orbits f_{disc}^* and the radial extent of the stars and gas in each galaxy, R_{90}^* and R_{gas} . To give an indication of how sensitive our results are to our definition of ‘disc’ stars having $\varepsilon \geq 0.5$, we also list the fraction of stellar mass with $\varepsilon \geq 0.7$.

While the FIRE-2 physics successfully reproduce observed relationships over a wide range of masses (see Hopkins et al. 2018,

and Section 1), our mass-selected sample does face some tension with observations. First, our galaxies are overly massive for their halo masses: our stellar mass definition places our sample between 0.2 and 0.55 dex above the Behroozi, Wechsler & Conroy (2013c) stellar mass *versus* halo mass relation (compared to the 0.218 dex scatter quoted by those authors at $z = 0$). Second, at these stellar masses, a non-negligible fraction of observed galaxies are quenched,

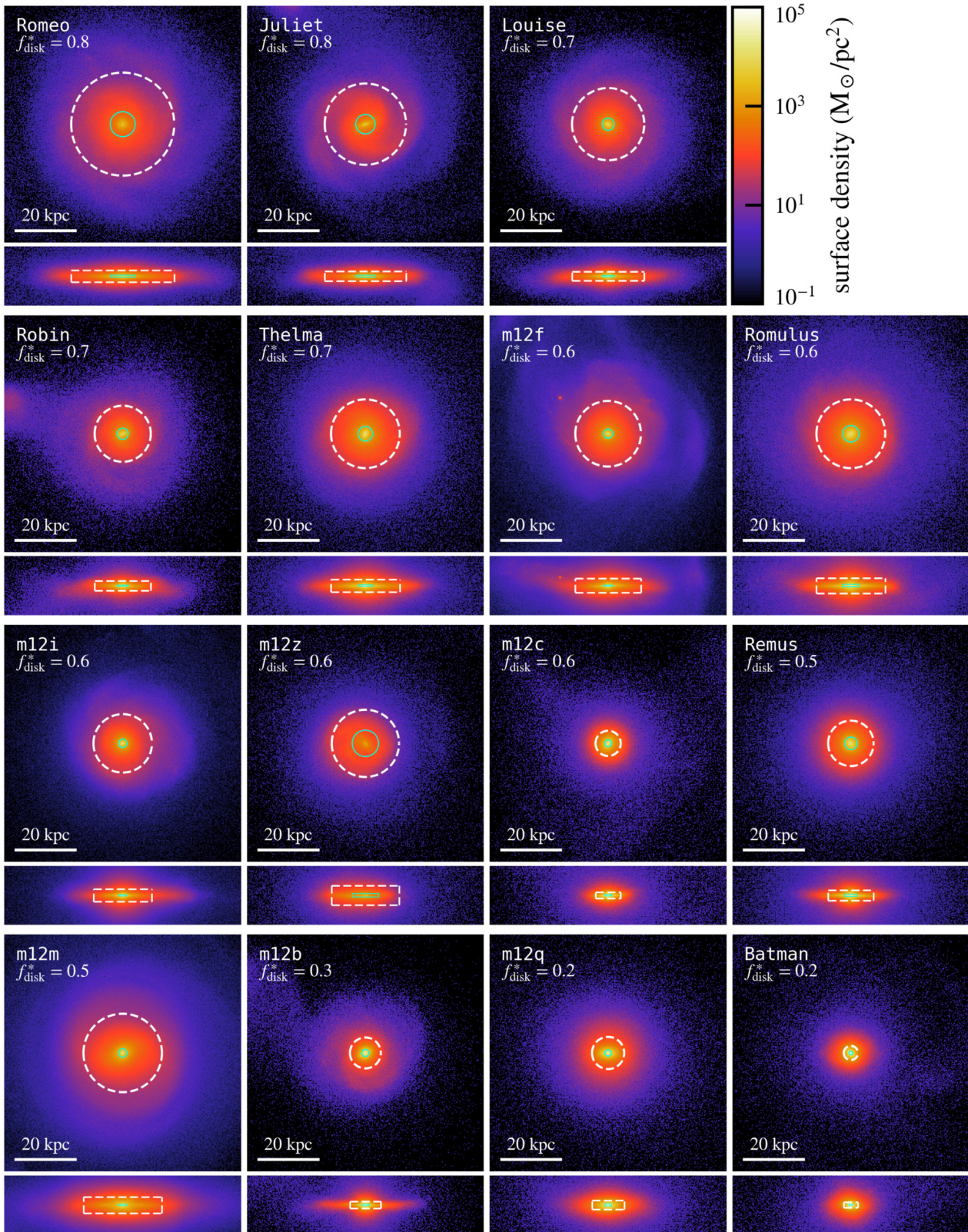


Figure 2. Face-on (top panels) and edge-on (bottom panels) projections of the stars in the FIRE-2 galaxies, colour coded by surface density, again sorted by decreasing f_{disc}^* , with the radius R_{90}^* and height Z_{90}^* that contain 90 percent of the mass indicated by the white circles/rectangles; the green lines show the equivalent half-mass quantities. Each panel is 80 kpc across; the edge-on projections are 20 kpc tall. Though there is not a direct correspondence between f_{disc}^* and disc size, they are clearly correlated (see Fig. 3).

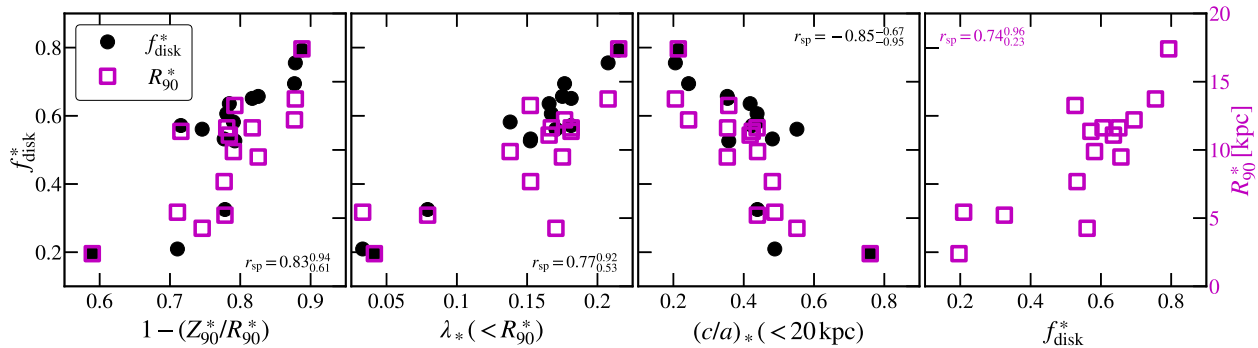


Figure 3. Comparing our adopted measures of morphology, f_{disc}^* (black points; left-hand axis) and R_{90}^* (open magenta squares; right-hand axis), to other spatial and kinematic measures of morphology, all measured at $z = 0$. The panels show $1 - (Z_{90}^*/R_{90}^*)$, a measure of the flatness of the stellar distribution; $\lambda_*(R_{90}^*)$, the Bullock, Kravtsov & Weinberg (2001) spin parameter of the stars in the galaxy; $(c/a)_*$, the ratio of the shortest to longest principal axes of the stars, measured within 20 kpc; and the disc fraction f_{disc}^* versus R_{90}^* . The r_{sp} values indicate the median Spearman r -coefficient obtained over 100 000 bootstrapping trials; the upper and lower values give the full 95 per cent confidence interval. In all but the final column (and in the remainder of this work), we compute the r -coefficient by combining the magenta squares and black circles; i.e. r_{sp} represents the joint correlation between the property on the x -axis and both f_{disc}^* and R_{90}^* (see equation 3.3 for details).

with strongly suppressed SFRs (e.g. Salim et al. 2007). However, none of the galaxies in our sample fall into this category: our lowest 100 Myr averaged specific SFR at $z = 0$ is $\sim 10^{-11.5} \text{ yr}^{-1}$ (possibly because these simulations do not include active galactic nucleus feedback; Bower et al. 2006; Cattaneo et al. 2006; Croton et al. 2006; Somerville et al. 2008). Though our sample includes only 15 galaxies, we caution that we may overproduce (or at least over-represent) late-type galaxies, which could potentially alter the correlations we present herein. Furthermore, if quenching correlates with properties of either the galaxy or the halo (e.g. the mass of the DM halo at fixed stellar mass; Woo et al. 2013) in a way not captured by the FIRE-2 models, then our analysis will miss those relationships.

3.3 Comparing morphological measures

Before examining correlations between various halo/galaxy properties, f_{disc}^* and the radial extents of our galaxies, we briefly explore the relationship between our morphological measures (f_{disc}^* and R_{90}^*) and other potential measures of morphology. As discussed in Sections 1 and 3.1, we do not explicitly compare with observational measures, as that lies beyond the scope of this work. However, we do note that the stellar radii that we adopt in this paper scale closely with the half-mass radii derived from fitting two-component Sérsic profiles to these same galaxies (Sanderson et al. 2017), though the bulge-to-disc ratios of those profiles do not correlate particularly well with the true kinematic disc fraction f_{disc}^* .

In addition to the properties we discuss above, there are a number of viable morphological definitions we could adopt, such as the angular momentum of the stars, the thickness of the stellar disc, or the shape of the stellar mass distribution. We examine how these properties correlate with f_{disc}^* and R_{90}^* in Fig. 3. In the first three panels, the filled black circles plot each quantity against f_{disc}^* (left y -axis), while the open magenta squares correspond to the right y -axis and indicate R_{90}^* . The final panel shows f_{disc}^* and R_{90}^* against one another and therefore omits the black points.

Any of these properties shown in Fig. 3 (along with other measures that we do not plot here, such as the stellar radius scaled by the virial radius, the specific angular momentum of the stars, the radius where the log slope of the stellar density profile equals -3 , or the kinematic bulge-to-disc ratio) are viable alternatives to f_{disc}^* and R_{90}^* . The correlations are unsurprising: at roughly fixed mass,

galaxies that are radially extended are also flatter, have larger stellar spin parameters, and have a greater fraction of rotation support. The final panel in Fig. 3 indicates the relationship between f_{disc}^* and R_{90}^* . As suggested by the visualizations in Fig. 2, the radial extent of the stars correlates with the degree of order in the disc, but with non-trivial scatter, motivating our analysis of both properties throughout.

The text in each panel (and in similar figures below) indicates the Spearman r -coefficient, r_{sp} , which quantifies the monotonicity of each relationship. We compute r_{sp} on the joint relationship with f_{disc}^* and R_{90}^* : we assign each galaxy a rank based on f_{disc}^* and a rank based on R_{90}^* , then combine those ranked data sets and compute r_{sp} against two copies of the ranked x -values of each plot. Our qualitative conclusions are unchanged if we compute r_{sp} against f_{disc}^* and R_{90}^* independently. For each relationship, we perform 100 000 bootstrapping trials (randomly drawing N points, with replacement). We report the median r_{sp} of those trials, and the values in superscripts and subscripts indicate the full 95 per cent confidence interval for those trials. We provide identical statistics throughout the remainder of this work. Based on the correlations reported in Fig. 3, which plots correlations between morphological properties that we expect to be reasonably well correlated, we adopt a rough criterion of $|r_{\text{sp}}| \gtrsim 0.8$, with a lower 95 per cent bound on the confidence interval of $|r_{\text{sp}}| \gtrsim 0.6$, as a ‘tight’ correlation.

Before turning to the drivers of stellar morphology, we briefly examine one non-parametric morphological measure that is relatively easy to measure in both simulations and observations: Σ_1 , the stellar surface density within the central 1 kpc (e.g. Cheung et al. 2012; Bell et al. 2012; Fang et al. 2013). For this mass-selected sample, we find a tight relationship between Σ_1 and morphology at $z = 0$: Fig. 4 shows Σ_1 as measured edge-on in open symbols and face-on in black circles. The viewing angle has a small impact, though edge-on projections are always higher, as expected. The anticorrelation between Σ_1 and the true morphology of a galaxy is striking, though somewhat unsurprising: for a roughly fixed stellar mass, galaxies with high central densities must be more compact, and Fig. 3 demonstrated that radial extent and degree of order in the stellar orbits are well correlated, again at fixed galaxy mass. We therefore conclude that Σ_1 is a reliable morphological measure, at least for roughly MW-mass galaxies. However, we caution that the low-lying outlier from the trend is m12 z, our lowest mass galaxy, suggesting the pos-

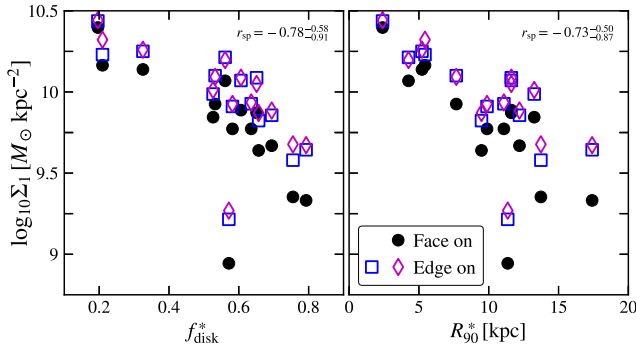


Figure 4. The stellar surface density within 1 projected kpc of the centre of the galaxy Σ_1 versus our adopted morphological measures, f_{disc}^* on the left and R_{90}^* on the right. Black circles show Σ_1 as measured from a perfectly face-on view, while the open symbols indicate Σ_1 measured along orthogonal edge-on projections. Regardless of viewing angle, the projected central density of the galaxy correlates strongly with both f_{disc}^* and R_{90}^* . The anticorrelation arises because higher central densities necessarily imply more compact (and therefore less discy) galaxies at fixed mass. The Spearman coefficients indicate the results of stacking all of the face-on and edge-on points together, though we find nearly identical values if we consider each separately.

sible emergence of a mass trend. Moreover, while some analyses have associated high Σ_1 with galactic quenching (e.g. Woo et al. 2015, 2017), all of our galaxies show some level of continued star formation to $z = 0$ (as noted above).

4 DRIVERS OF STELLAR MORPHOLOGY

We now turn to correlations between stellar morphology, quantified primarily by f_{disc}^* and R_{90}^* , and various properties of the galaxy and the host halo, both in the hydrodynamic simulation and in the analogous DMO run. In short, we search for physical drivers of and explanations for the $z = 0$ morphologies of each of the galaxies in our sample.

4.1 Mass (around MW masses)

We begin by checking whether the morphologies of the FIRE-2 MW-mass galaxies are driven by either the halo or galaxy mass. Fig. 5 indicates the virial mass M_{vir}^* , the stellar mass M_{galaxy}^* , the gas mass M_{gas}^* , and the total gas mass within R_{vir} , all at $z = 0$. As in Fig. 3, black points correspond to the left-hand axis and plot f_{disc}^* , while magenta squares indicate R_{90}^* (right-hand axis). Of the masses shown in Fig. 5, only $M_{\text{galaxy}}^{\text{gas}}$ displays evidence for a correlation with the $z = 0$ stellar morphology. Though we do not plot it, we also find no correlation between the total baryonic mass within R_{vir} and kinematics/morphology ($r_{\text{sp}} = -0.6$ to 0.06). There is evidence for a correlation with the total mass in cold gas (defined as $T < 10^5$ K) within R_{vir} ($r_{\text{sp}} = 0.52$ – 0.85), but because the cold gas is predominantly in the galaxy, this correlation is driven by $M_{\text{galaxy}}^{\text{gas}}$.¹⁰ We will return to the correlation with $M_{\text{galaxy}}^{\text{gas}}$ below, but here we emphasize that the morphologies of the MW-mass FIRE-2 galaxies do not correlate with either the halo mass, the stellar mass of the galaxy, or the total baryonic mass within R_{vir} . Note that over a large

¹⁰Conversely, nearly all of the gas defined as ‘in the galaxy’ has $T > 10^5$ K. Batman has the *lowest* ‘galaxy cold gas fraction’ with $M_{\text{gas}}(R < R_{\text{gas}}, Z < Z_{\text{gas}}, T < 10^5 \text{ K})/M_{\text{gas}}(R < R_{\text{gas}}, Z < Z_{\text{gas}}) = 0.977$.

dynamic range, however, there is a strong mass dependence (e.g. El-Badry et al. 2018 showed that the FIRE-2 dwarfs are spherical and dispersion dominated).

4.2 Spin (and other DM properties)

As discussed in Introduction, many authors have pointed out that, if baryons acquire their angular momentum from their DM haloes and begin with the same density profile as those haloes, then the size of the stellar disc should be predicted by a combination of the Peebles (1969) spin parameter λ_{Peebles} , the size of the host halo, the fraction of angular momentum in the halo that resides in the disc j_d , and the fraction of halo mass that resides in the disc m_d . In the model of Fall (1983), wherein the galaxy is hosted by a static isothermal sphere,

$$R_d = 2^{-1/2} (j_d/m_d) \lambda_{\text{Peebles}} R_{200}. \quad (1)$$

In the more complete model of Mo et al. (1998), where the disc grows adiabatically within an initially NFW (Navarro et al. 1996) halo, the disc radius is modified by two multiplicative functions; the first arises from the change in the total energy of the NFW profile relative to an isothermal sphere and the second from the (assumed) adiabatic contraction of the halo in response to the growth of the disc. If such a relationship is borne out by the FIRE-2 simulations, and if $j_d/m_d = j_{\text{disc}}/j_{\text{halo}}$, the ratio of the specific angular momentum of the disc to the halo, is roughly constant (i.e. if the baryons acquire their angular momentum from the halo, as assumed in Fall 1983), then one can accurately populate haloes in DMO simulations with galaxies of the proper size and, by virtue of the correlation between R_{90}^* and f_{disc}^* , roughly the proper disc fraction. Moreover, validation of the model would provide evidence for the overall theory of angular momentum-regulated disc growth.

Fig. 6 tests this picture by comparing the half-mass radius predicted by the models of Fall (1983) and Mo et al. (1998) to the half-mass radius of each simulated galaxy. Circles show the results of the isothermal model (equation 1), and squares plot the full model assuming an adiabatically contracted NFW halo (equation 28 of Mo et al. 1998). In order to test the assumption that galaxies acquire their angular momentum from the DM, the left-hand panel uses properties available from the DMO simulations and fixes $j_d = m_d$.¹¹ Given the relatively small variations in R_{200} within our sample, the left-hand panel implicitly tests whether disc size is driven by the spin of the halo at $z = 0$. Neither model is able to reproduce the actual size of our galaxies, in line with the general results of zoom-in simulations discussed in Introduction. The bracketed numbers in the legends indicate the average fractional error of each set of points relative to the simulations: the isothermal Fall (1983) model dramatically overpredicts the size of the galaxies when assuming $j_d = m_d$. The contracted-NFW halo model produces a reasonable order-of-magnitude estimate of R_{50}^* , but the actual predictive value is quite poor.

The right-hand panel frees the assumption that the angular momentum of the galaxy is correlated with the spin of the halo and instead fits the galactic angular momentum independently by adopting j_d and m_d (along with the remainder of the halo properties) from the hydrodynamic simulations. We calculate j_d (m_d) from the simulations as the ratio of the stellar angular momentum (mass) within R_{90}^* to the total angular momentum (mass) within R_{200} . By doing so,

¹¹We adopt $j_d = m_d = 0.1$, but our overall results are insensitive to the chosen value.

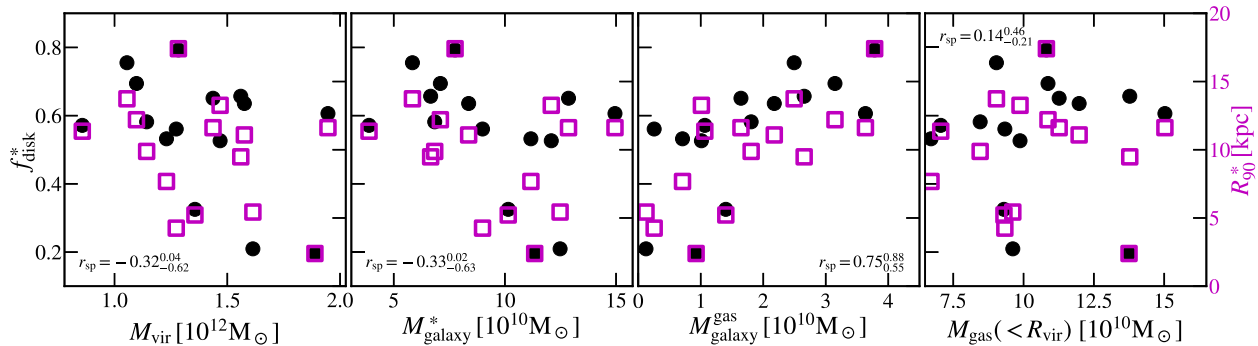


Figure 5. The $z = 0$ relationship between our morphological measures and, (a) the virial mass of the halo M_{vir} , (b) the stellar mass of the galaxy M_{galaxy}^* , (c) the gas mass within the galaxy $M_{\text{galaxy}}^{\text{gas}}$, and (d) the total gas mass within R_{vir} . Morphology in the FIRE-2 simulations is not correlated with either M_{vir} , M_{galaxy}^* , or the total gas mass within R_{vir} , across this narrow mass range, but gas-rich galaxies are more likely to be discy today; we discuss this correlation in more detail below.

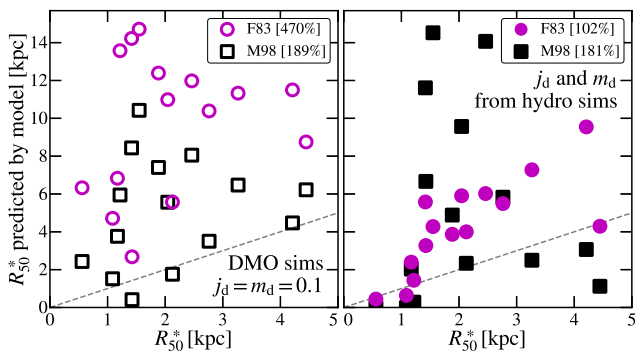


Figure 6. The half-mass radius of the FIRE-2 galaxies *versus* the half-mass radius predicted by the Fall (1983, isothermal) and Mo et al. (1998, NFW) models for each galaxy (see equation 1). Circles show results assuming an isothermal potential, and squares indicate the model with an adiabatically contracted NFW profile. The left-hand panel uses the properties of the halo available in the DMO simulation (fixing $j_d = m_d$), and therefore tests the assumption the small variations in R_{200} in our sample). The right-hand panel frees this assumption by adopting j_d and m_d from the hydrodynamic simulations, and instead tests whether the galaxies are well described by a rotationally supported disc in a fixed potential. The numbers in brackets indicate the average fractional error of the model relative to the simulations.

we measure the true angular momentum of the galaxy (i.e. independent of the spin of the halo) and therefore test the assumption that a rotationally supported disc in a fixed gravitational potential (determined by a simple NFW or isothermal model) provides a reasonable approximation. Even under this assumption, the predictions are only moderately accurate, though we do find order-of-magnitude agreement across this mass range, in line with observational results that show a correlation between virial radius (i.e. halo mass) and galaxy size (e.g. Kravtsov 2013). The relative success of the isothermal model (compared to the NFW model) may suggest that the density profiles are closer to isothermal spheres at their centres, but we see no strong evidence in the actual profiles (though see Chan et al. 2015, who found that the total density profiles at the centres of MW-mass FIRE-1 galaxies are well fitted by an isothermal sphere).

Though we adopt all of the halo parameters in the hydrodynamic simulation in the right-hand panel (R_{200} , λ_{Peebles} , c , j_d , and m_d), the majority of the changes are driven by allowing j_d and m_d to vary freely and independently: even for our sample of 15 galaxies, j_d , m_d , and their ratio vary by nearly an order of magnitude: $0.005 \lesssim$

$j_d \lesssim 0.07$, $0.04 \lesssim m_d \lesssim 0.09$, and $0.1 \lesssim j_d/m_d \lesssim 0.75$ (also see Posti et al. 2018, who showed that the variance in $M_{\text{galaxy}}^*/M_{\text{vir}}$ with M_{vir} , together with the relationship between M_{galaxy}^* and the stellar specific angular momentum observed in Fall 1983, imply that the ratio of the stellar-to-halo specific angular momentum must also vary). Galaxies acquire a broad range of the specific angular momentum available in their hosts, and one must know the true j_d and m_d in order to even roughly predict the radial extent of a given galaxy with the Fall (1983) or Mo et al. (1998) models. We are unable to recover a tight correlation with a single value of j_d and m_d for all galaxies (even when $j_d \neq m_d$). There is some evidence for a correlation between j_d and the 1Mpc environment: the median j_d of the galaxies in Local Group-like pairs is twice that of the isolated sample. Accordingly, six of the seven disciest galaxies in our sample are in Local Groups. However, our sample size is too small to make definitive statements.

In our parameter exploration, we have generally found that, of the properties of the entire $z = 0$ DMO halo, λ (or λ_{Peebles}) correlates most tightly with morphology ($r_{\text{sp}} = 0.05 - 0.7$ for the latter)¹² though the correlation is weak with a large degree of scatter about the average relationship: our largest, most ordered galaxy has an average spin parameter. While $\lambda(z = 0)$ is relatively stable between the DMO and baryonic simulations,¹³ λ_{DMO} alone is insufficient to predict morphologies without alleviating the scatter by multiplying by the true values of j_d and m_d .

Strictly speaking, the Fall (1983) and Mo et al. (1998) models should only apply to the rotation-supported material, and should make no distinction between the gas and stars: equation (1) should predict the scale radius of the exponential disc formed by all of the rotating material. Though we are generally interested in predicting the complete morphology (e.g. the fraction of rotating material, rather than just the extent of that material), we have checked whether these models recover the size of the rotating baryons, which we define strictly here as mass with $\varepsilon \geq 0.75$. The models perform significantly better at recovering these sizes, particularly if j_d and m_d are taken from the hydrodynamic simulations,¹⁴ as expected from the fact that only the profile remains an

¹²However, see Section 4.9.1, where we discuss correlations with the properties of the *inner* DM halo.

¹³The average fractional difference in our sample is ~ 1 per cent.

¹⁴The isothermal model is accurate to within an average of 3 per cent at predicting the half-mass radius of all the rotating baryons.

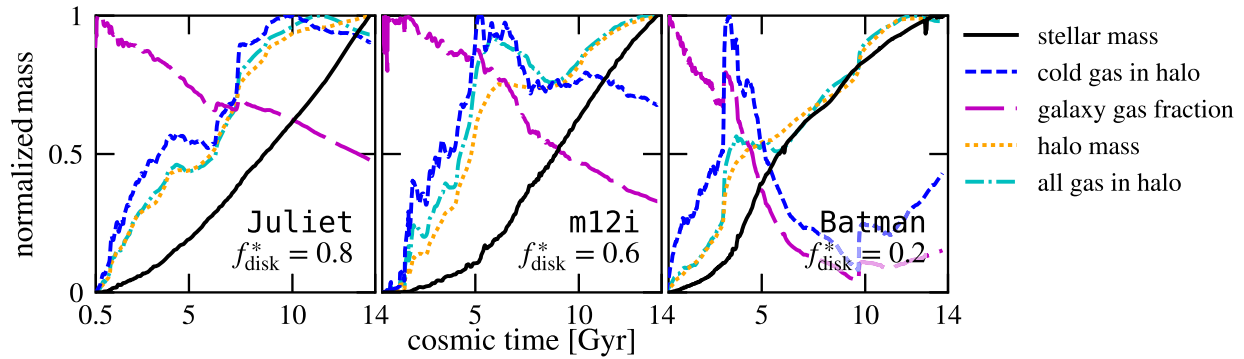


Figure 7. Evolutionary histories of three representative galaxies; the entire sample is shown in Appendix C. Each curve is normalized to its maximum value. The clearest trend, which holds generically for our sample, is that galaxies that have higher cold gas fractions and more gas available to form stars at late times (relative to their mass at early times) form the majority of their stars in discy configurations. This follows directly from the fact that star formation is chaotic and bursty at high redshift, but settles into an ordered, disc-like configuration after $z \sim 1$ (for most galaxies that will be MW mass at $z = 0$). We quantify these trends for the full sample in Fig. 8.

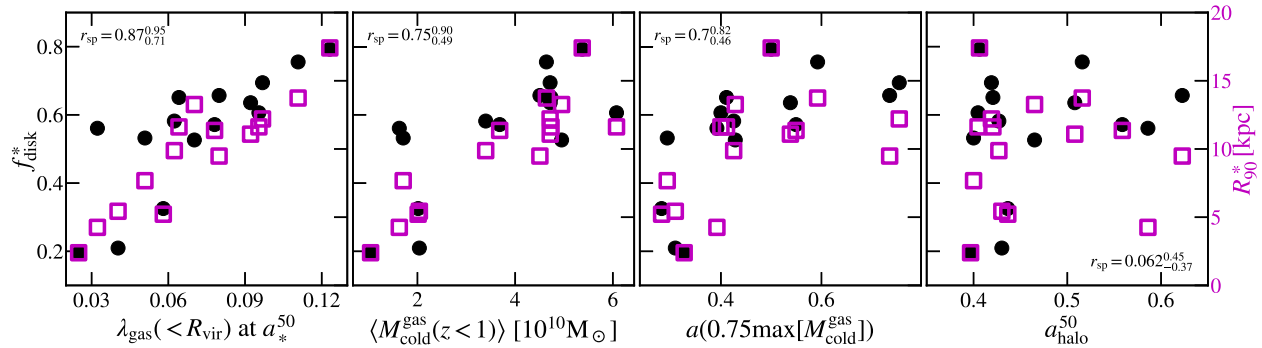


Figure 8. The morphologies of our galaxies as a function of several parameterizations of the gas accretion histories of our galaxies and their host haloes. In order, the columns plot the spin parameter λ of the gas within R_{vir} at the scale factor when half of stars in the galaxy at $z = 0$ formed a_*^{50} , the average amount of cold gas in the halo after $z = 1$, the scale factor at which the cold gas in the halo first reaches 75 per cent of its peak, and the scale factor at which the halo reaches 50 per cent of its mass a_{halo}^{50} . The first three, which contain information about the accretion history and buildup either of the galaxy itself or of material that helps to build the galaxy, all correlate reasonably tightly with $z = 0$ morphology: the first panel is actually the tightest correlation we have identified. The final column, however, indicates that the history of the DM is less meaningful: the DM accretion history and halo merger history contains little information about the $z = 0$ morphology (also see Section 4.9).

assumption in that case. When j_d and m_d are not known and the spin parameters from the DMO simulations are adopted, the agreement remains reasonably good on average (32 per cent when using the Mo et al. 1998 model, but 156 per cent with the Fall 1983 model).

Overall, we emphasize that neither the Fall (1983) nor the Mo et al. (1998) model accurately predicts the total galactic morphology. This result is in apparent tension with that of Grand et al. (2017), for example, who found a positive correlation between the halo spin (in a hydrodynamic simulation) and their ‘disc scale length’. However, we caution that the R_{50}^* plotted in Fig. 6 differs from the disc length used in that work, which was calculated by fitting two-component profiles to the stellar surface density near the disc such that bulge (dispersion-supported) stars do not contribute to the scale length. In fact, we do find a (weak) positive correlation between the half-mass radius of the rotation supported stars and the spin of the halo: $r_{\text{sp}} = 0.02\text{--}0.8$.

Given the apparent difficulty of predicting the morphology of a galaxy with only the information available about the host halo in a DMO simulation, we therefore turn our attention to identifying physical drivers of the morphology in the hydrodynamic simulations. That is, we do not attempt to predict morphologies,

but rather to explain them through galactic/halo properties at all redshifts.

4.3 Gas fraction and accretion history

Figs 7 and 8 represent the culmination of these searches. The former, Fig. 7, shows the normalized mass accretion histories of three representative galaxies, Batman, m12i, and Juliet (growth histories for the full sample are plotted in Appendix C). The black curves indicate the stellar mass within R_{90}^* , the blue curves show the total cold gas within R_{vir} (where ‘cold’ is again defined as $T < 10^5$ K), and the magenta curves indicate the ratio of the cold gas mass to the stellar mass of the galaxy (i.e. the ratio of the black and blue curves without normalizing). Finally, the cyan and orange curves indicate the total gas mass within R_{vir} and the total halo mass, respectively. Each curve is normalized to its maximum value. We find qualitatively identical results measuring the total gas mass near the galactic centre via the same iterative process we adopt for the stars: the vast majority of the cold gas in the halo at any given time is in the galactic disc. However, we opt to use the total cold gas mass within the virial radius, $M_{\text{cold}}^{\text{gas}}$, because this iterative process can falsely capture hot gas in the halo, as discussed earlier.

Of course, every galaxy has a unique evolutionary history, and our results suggest that history is instrumental in shaping the $z = 0$ galaxy. However, there are trends that hold generically across our sample, which are exemplified by the three panels in Fig. 7. First, while the total gas in the halo closely tracks the total halo mass for all galaxies, the behaviour of the cold gas in the halo, i.e. the fuel for star formation, varies strongly with f_{disc}^* . Galaxies similar to `Batman` with low f_{disc}^* tend to reach their maximum cold gas mass at early times (both in absolute terms and in comparison to the growth of their DM haloes) when star formation is chaotic and bursty, and quickly exhaust (or heat) that gas. They therefore form more stars with bulge-like configurations, and stars that are formed in a disc are subject to greater dynamical disruption from the powerful feedback events. Galaxies that reach their maximum cold gas mass at early times but maintain a relatively large reservoir for star formation until late times, either through mergers or accretion from the circumgalactic medium (CGM), form a similar fraction of stars during the bursty period and at late times ($z \lesssim 1$), when the star-forming gas has settled into a rotation-supported disc, as is the case with `m12i`. Finally, galaxies such as `Juliet` that are disc-dominated tend to have relatively little gas and form relatively few stars during the bursty phase. These trends are also evident in the gas fractions: bulge-dominated systems tend to reach gas fractions $\lesssim 0.25$ at or before $z \sim 1$, while disc-dominated systems maintain high gas fractions until late times.

4.4 Galaxy mergers

Second, comparing the evolution of `Batman` and `Juliet` reveals the varying impacts of mergers on the $z = 0$ morphologies. `Batman`, which experiences a double merger at $z \sim 2$ ($t \sim 3$ Gyr; revealed by the sharp uptick in M_{vir}) when the halo mass is relatively low, has a large amount of cold gas dumped into the halo. That gas then forms nearly half of the $z = 0$ stellar mass over the next ~ 1 – 2 Gyr, the majority of which ends up as a compact, dispersion supported system. Other bulge-dominated galaxies in our sample typically experience similarly large mergers at early times (when the systems have $M_{\text{vir}} \ll 10^{12} M_{\odot}$ and therefore no extended ‘hot haloes’ of gas; see e.g. Kereš et al. 2005). Those mergers then tend to funnel their gas into the centre of the galaxy relatively rapidly (Barnes & Hernquist 1991; Bournaud et al. 2011; Zolotov et al. 2015). Mergers that occur later (when the hot halo is in place), however, tend to have their gas gradually stripped off and incorporated into the central galaxy more gradually. `Juliet`, for example, has a gas-rich halo fall inside the virial radius at $z \sim 1$, but the gas in that subhalo is slowly stripped off and accreted onto the central disc over the course of several pericentric passages, feeding an extended star-forming disc.

Overall, visual inspection of the movies of our simulations (<http://www.tapir.caltech.edu/~sheagk/firemovies.html>) indicates that large *galactic* mergers do typically lead to bulges in our sample. This is particularly true if those mergers occur on first infall (i.e. with low angular momentum), before the gas in the merging system can be gradually stripped and mixed with the halo, then more gently added on to the host (in agreement with the results of Sales et al. 2012 regarding morphology as a function of the dominant gas accretion mode). The prominent bulges of `Batman`, `m12q`, `m12b`, and `Remus`, for example, were all created by such events. However, the sizes of the bulges built by these events varies: `Robin` experiences such a merger at $z \sim 2$, but the overall masses were low at that time, leading to a small bulge relative to the disc that grows later.

Because a small fraction of the stellar mass in the central galaxy is formed *ex situ* (i.e. brought in by mergers; typically less than 5 per cent), they do not significantly contribute directly to f_{disc}^* (also see Anglés-Alcázar et al. 2017). The actual *ex situ* fraction is also not correlated with morphology ($r_{\text{sp}} = -0.3$ to 0.55), and in the majority of our sample, the deposited *ex situ* stars are typically dispersion supported. However, a few galaxies in our sample have accreted stars that contribute to the disc: three galaxies have their *ex situ* circularity distributions peak at $\varepsilon \sim 0.6$, and in particular, our two disciest galaxies have even their accreted stars on discy orbits with ε peaking at ~ 0.9 and 1 .

4.5 Secular evolution and bulges

Not all bulges are built by mergers, however: neither `m12m`, `m12i`, nor `Louise` experience a major head-on galactic merger, but all host dispersion-supported stars today. The bulge in `m12m` is built by a secular bar-buckling event (Debatista et al. 2018). Meanwhile, `m12i` hosts a compact gas disc that initially loses angular momentum in a series of mergers, but then slowly builds up a larger disc at late times. Therefore, systems that have undergone direct galactic mergers are more likely to host a bulge than compared to those evolving just under secular evolution (internal effects), but the exact morphology depends on the interplay between the merger history, star formation history, and angular momentum of the gas that builds the disc.

4.6 Clump sinking/migration

Both observations (e.g. Förster Schreiber et al. 2011, and references therein) and simulations (e.g. Mandelker et al. 2017) of star-forming, discy galaxies at $z \sim 2$ have found evidence for large ($\sim 10^7$ – $10^9 M_{\odot}$) gas clumps that may migrate to the centres of their host discs to form secular bulges. However, the galaxies we study here are low enough mass at $z \sim 2$ that we simply do not expect or see this channel of bulge formation. Moreover, we note that Oklopčić et al. (2017) showed that while giant clumps do form in massive galaxies at $z \sim 2$ in the FIRE simulations, there was no evidence that these clumps have a net inward migration inwards that build a bulge, even at higher masses than we study here.

4.7 Misalignments and counter-rotating discs

By examining the angular momentum of the material that end up in the galaxy and halo at turnaround ($z \sim 3.5$), Sales et al. (2012) argued that disc-dominated galaxies are typically formed out of well-aligned material, while bulge-dominated systems are more likely to experience misaligned accretion events. We see some evidence for this picture in our sample: `m12q`, in particular, is formed out of the merger of two counter-rotating discs at $z \sim 0.8$, and `Batman` and `m12b` also experience large, misaligned galactic mergers.

However, in our sample, this effect manifests primarily through mergers, and it therefore has either a dramatic impact or a nearly negligible one: the fraction of counter-rotating stellar mass ($\varepsilon \leq -0.5$) at $z = 0$ is less than 4 per cent in the remaining 12 galaxies and, as we show in Section 5.2, the fraction that *forms* counter-rotating is even smaller. Moreover, Section 5.2 demonstrates that the fraction of stars that form in a bulgy configuration ($|\varepsilon| < 0.5$) is relatively smooth across our sample, suggesting a minor (or relatively constant) contribution from misaligned gas that forms stars before integrating with the disc. However, our results do not preclude the possibility of misaligned accretion contributing to torquing the disc

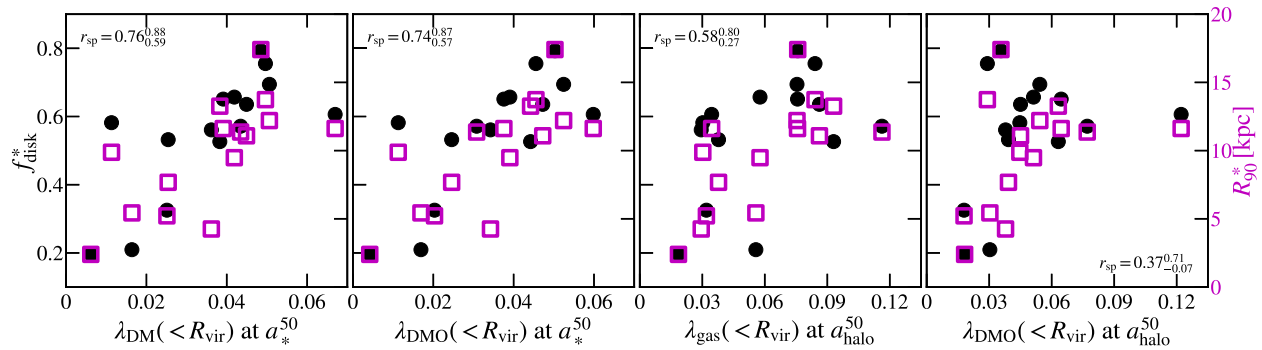


Figure 9. Galactic kinematics and morphology as a function of the spin parameter, measured at the time (scale factor) when half of the stars in the galaxy have formed, a_*^{50} (left two panels, as in the left-hand panel of Fig. 8), and at the time (scale factor) when the halo reached half of its $z = 0$ mass, a_{halo}^{50} (right two panels). The relationships with the spin parameter of the DM at $a = a_*^{50}$, either in the baryonic or DMO run, shows more scatter than with the gas, but only marginally so. However, the spin parameters at $a = a_{\text{halo}}^{50}$ (whether gas or DMO) are only weakly correlated with morphology, at best, emphasizing the difficulty of predicting galactic morphology given only a DMO simulation.

and shifting stars to lower circularities. Together with the large scatter in the trend identified by Sales et al. (2012), we conclude that our results are in overall agreement with theirs.

4.8 Summary: the evolution of the gas mass and spin

We quantify these trends in Fig. 8. As in Figs 3 and 5, the black circles show f_{disc}^* and the magenta squares indicate R_{90}^* . From left to right, the x -axes plot the spin parameter of the gas in the halo at the scale factor a_*^{50} when half of the $z = 0$ stellar mass had formed, the average cold gas mass within the halo after $z = 1$, the scale factor when $M_{\text{cold}}^{\text{gas}}$ first reaches 75 per cent of its peak, and the scale factor when the halo mass reaches half of the $z = 0$ value, a_{halo}^{50} . The first three are positively, and relatively strongly, correlated with morphology: the spin parameter of the gas at a_*^{50} is actually the tightest (non-morphological) correlation we have identified, and $\langle M_{\text{cold}}^{\text{gas}}(z < 1) \rangle$ displays the tightest relationship outside of other related spin parameters. In fact, $\langle M_{\text{cold}}^{\text{gas}}(z < 1) \rangle$ is even more tightly correlated with morphology than the spin parameter of the gas in the halo at $z = 0$, which has $r_{\text{sp}} = 0.31\text{--}0.81$. We find similar correlations for other descriptions of the gas accretion history of the halo, such as the scale factor when the total gas mass within 30 kpc first reaches 75 per cent of its maximum.

Together, Figs 7 and 8 suggest that disc-dominated galaxies are formed in systems that maximize their star-forming reservoir at late times (often via fresh gas delivered by infalling subhaloes), and where the gas that will turn into stars at late times has a high spin. These conditions often coincide – gas that infalls at late times, whether through mergers or smooth accretion, tends to have a higher impact parameter and therefore more angular momentum than similar interactions at early times (White 1984; Peirani, Mohayaee & de Freitas Pacheco 2004; Kereš & Hernquist 2009; Stewart et al. 2011; Pichon et al. 2011; Stewart et al. 2013; Lagos et al. 2017; Stewart et al. 2017). This picture is also largely consistent with the results of previous theoretical and observational works, which have generally found that stellar discs form inside-out and are composed of young stars, while the oldest stars reside in the galactic bulge (Kepner 1999; Pilkington et al. 2012; Howes et al. 2015). It is also relatively unsurprising based on the colouring in Fig. 1, which indicates that the youngest stars in each galaxy have disc-like kinematics. Unfortunately, it further reinforces the discussion above that it is difficult to accurately predict the $z = 0$ morphology of a galaxy that will form in a given halo based on a DMO simulation, as the

morphology is primarily driven by the gas dynamics. The ubiquity of galactic winds and gas recycling in the FIRE simulations further complicates efforts to connect DMO simulations to the galactic morphology/kinematics (Anglés-Alcázar et al. 2014; Muratov et al. 2015; Anglés-Alcázar et al. 2017).

Any individual bulge, meanwhile, can be sourced by either mergers or secular processes, and both contribute significantly. However, the former are more important at early times, while the latter typically lead to later bulge formation. In fact, when mergers happen at later times in our sample, they tend to be smaller, gas-rich galaxies merging onto the central host and depositing more gas at larger radii, enhancing the chance of disc survival (consistent with Hopkins et al. 2009b). In our limited sample, however, there is no obvious way to attribute all morphological trends to ‘merger history’ or to ‘bar formation’.

4.9 Predicting morphology from DM-only properties

To emphasize the difficulty of using a DMO simulation to a priori estimate the morphology of a galaxy in light of the tight correlation between λ_{gas} at a_*^{50} (which suggests that a similarly tight correlation might exist for λ_{DMO} at some $z > 0$), Fig. 9 shows galactic morphology against various spin parameters at two scale factors: a_*^{50} and a_{halo}^{50} , the half-mass time of the total halo mass; only the latter is available in a DMO simulation. The first panel shows the spin parameter of the DM in the baryonic simulation at a_*^{50} . While it is less tightly correlated with morphology than the spin parameter of the gas in the halo at the same scale factor (Fig. 8), the relationship remains relatively tight. The second panel demonstrates that the correlation between the DM spin (at a_*^{50}) and morphology is not driven by interactions between the baryons and the DM – the spin parameter in the DMO simulation at the same scale factor also correlates with morphology, though again less strongly.¹⁵ However, those correlations have not yet appeared at the (earlier) a_{halo}^{50} : the third panel shows that the spin parameter of the gas at a_{halo}^{50} is only weakly correlated with morphology, and the final panel illustrates

¹⁵Though we have not identified any direct correlations between DMO halo properties and a_*^{50} , the relationship in the second panel suggests that, if one could predict the galaxy half-mass time from a DMO simulation alone, there may be a path from the properties of the halo in the DMO simulation to the galactic morphology.

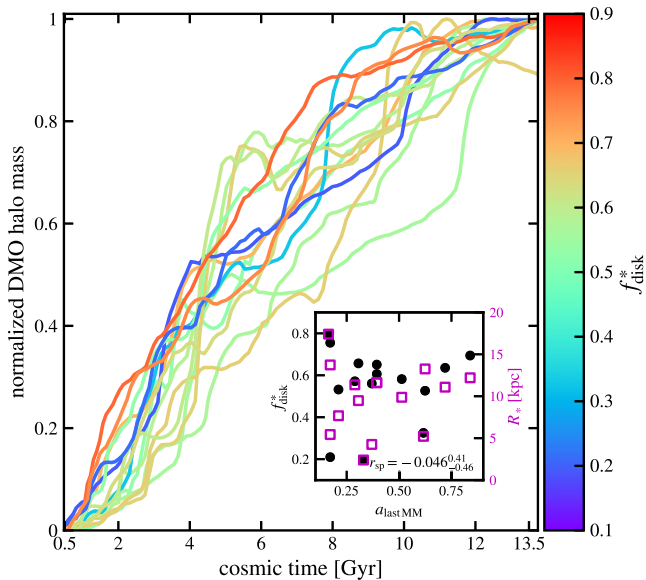


Figure 10. The normalized mass accretion histories of our host haloes in the DMO simulation. The inset shows the scale factor of the last major merger (defined as a mass ratio of ≥ 0.3) in the DMO simulation against galactic morphology. While the galaxies with the largest bulges do tend to reside in haloes that form early, the most disc-dominated systems have actually accreted a greater fraction of their mass by $z \sim 1$ ($t \sim 6$ Gyr). Moreover, there is effectively no correlation between the timing of the last major merger and morphology.

that the spin parameter in the DMO simulation contains little information at this time (as it does at $z = 0$). We also note that λ_{gas} is typically 2–3 times the spin of the DM (both at high z and at $z = 0$; first pointed out by Stewart et al. 2011), emphasizing the disconnect between the angular momentum of the baryons (particularly those that eventually form the galaxy) and the halo. Moreover, while there is a reasonably tight correlation between a_*^{50} and $a_{\text{halo, DMO}}^{50}$ ($r_{\text{sp}} = 0.4\text{--}0.92$), a direct route from DMO halo properties to galaxy morphology would require a similar correlation between $\lambda_{\text{gas}}(a = a_*^{50})$ and $\lambda_{\text{DMO}}(a = a_{\text{halo, DMO}}^{50})$, which we see no strong evidence for ($r_{\text{sp}} = -0.22$ to 0.85).

We also explore trends with the accretion history of the main branch of the DMO halo in Fig. 10. The inset panel shows the scale factor of the last major merger in the DMO run against the galactic morphology.¹⁶ The curves are coloured by f_{disc}^* ; the most bulge-dominated galaxies tend to have higher masses at early times, but the haloes that host the galaxies with the highest $z = 0$ disc fractions in our sample typically have even higher (normalized) masses at any $z \gtrsim 1$. This is similar to the result in Fig. 8: the evolution (and spin parameter) of the halo contains relatively little information about the galactic morphology compared to the evolution (and spin parameter) of the galaxy itself.

4.9.1 Inner DM halo properties

As noted in Introduction, some authors have argued for a correlation between the inner DM halo (typically within $r \sim 0.1R_{\text{vir}}$) and the morphology (or at least the orientation) of the galaxy (e.g.

¹⁶Merger times and mass accretion histories are drawn from merger trees built with `consistent-trees` (Behroozi et al. 2013b) using `rockstar` (Behroozi, Wechsler & Wu 2013a) halo catalogues.

Bailin & Steinmetz 2005; Bett et al. 2010; Zavala et al. 2016). We have therefore checked for correlations between properties of the inner DM halo (which we define as within $0.1R_{\text{vir}}(z)$), both in the hydrodynamic and DMO simulations, at $z = 0$ and the two scale factors at which spins parameters are plotted in Fig. 9.

Overall, we find that the properties of the DM in the central portion of the halo do correlate more strongly with the galactic morphology. This is particularly true when examining halo properties in the hydrodynamic simulations, where the formation of the galaxy can impact the dynamics of the DM: for example, we find that the spin parameter of the DM (in the hydro run) within $0.1R_{\text{vir}}$ of the galaxy is reasonably well correlated with the morphology of that galaxy: $r_{\text{sp}} = 0.32\text{--}0.82$. We also reproduce the result of Zavala et al. (2016) that specific angular momentum in the inner DM halo ($j_{\text{DM}}(< 0.1R_{\text{vir}})$) correlates with that of the stars (j_*) at $z = 0$: we find $r_{\text{sp}} = 0.65_{0.29}^{0.86}$, whereas those authors report $r_{\text{sp}} = 0.5$, within our confidence interval.

The properties of the inner halo in the DMO simulations also offer slightly better options for predicting the galaxy morphology than when using the entire halo, but scatter remains in all the relationships. Most notably, we find a marginally higher Spearman coefficient between galaxy morphology and the specific angular momentum of the DMO halo within $0.1R_{\text{vir}}$ at $z = 0$ ($r_{\text{sp}} = 0.32\text{--}0.81$) than with the spin parameter of the entire halo. Moreover, the Fall (1983) and Mo et al. (1998) predictions are more accurate when the spin parameter at $0.1R_{\text{vir}}$ is used: we find average fractional errors of 280 per cent (isothermal) and 62 per cent (NFW). Together, these results suggest that the inner DM halo may hold clues to galactic morphology, even without the galaxy impacting the evolution of the DM.

4.10 Other

In addition to the properties shown in Figs 5, 8, 9, and 10 and discussed above, we have also checked for correlations with numerous other parameters of the galaxy, halo, or DMO halo both at $z = 0$ and at higher redshifts, including their growth histories. Examples of those that correlate with the $z = 0$ morphology, but less strongly than those we present above, include properties associated with the star formation history, such as the amount of time that the galaxy maintains a (200 Myr averaged) SFR of at least 50 per cent of its peak value and the fraction of stars formed during that time. Similarly, the actual peak SFR shows a weak anticorrelation: relatively constant, extended star formation is more likely to create a well-ordered disc (as discussed in Muratov et al. 2015). However, the scale factor when the galaxy reaches its peak SFR is uncorrelated with morphology today ($r_{\text{sp}} = -0.33$ to 0.54). The fraction of specific angular momentum in the disc, $j_{\text{d}}/m_{\text{d}}$, is also weakly correlated with $z = 0$ morphology, as is the spin of the gas/halo at $z = 1$.

Finally, a non-exhaustive list of properties that show no statistically significant signs of correlation with f_{disc}^* or R_{90}^* include (along with their associated bootstrapped 95 per cent CI on r_{sp}) includes:

- (i) $M_{\text{galaxy}}^*/M_{\text{vir}}$ ($r_{\text{sp}} = -0.49$ to 0.11),
- (ii) the total angular momentum in the DMO halo at $z = 0$ ($r_{\text{sp}} = 0.09\text{--}0.48$),
- (iii) the NFW scale radius of the DMO halo at $z = 0$ ($r_{\text{sp}} = -0.52$ to 0.14),
- (iv) the $z = 0$ shape of the DMO halo at various radii ($r_{\text{sp}} = 0.14\text{--}0.5$ at 10 kpc and $r_{\text{sp}} = 0.08\text{--}0.64$ at 300 kpc),

- (v) the fraction of M_{vir} in bound subhaloes at $z = 0$ ($r_{\text{sp}} = -0.18$ to 0.54),
- (vi) the scale factor at which the SFR peaks ($r_{\text{sp}} = -0.32$ to 0.52),
- (vii) the $z = 0$, 100-Myr-averaged SFR ($r_{\text{sp}} = -0.34$ to 0.52) and specific SFR ($r_{\text{sp}} = -0.27$ to 0.52),
- (viii) the fraction of stellar mass formed after $z = 1$ ($r_{\text{sp}} = -0.25$ to 0.44),
- (ix) the fraction of halo mass accreted after $z = 1$ ($r_{\text{sp}} = -0.27$ to 0.31),
- (x) the fraction of *in situ* stars within 30 kpc ($r_{\text{sp}} = -0.3$ to 0.55),
- (xi) the mass of the stellar halo, whether selected by $z = 0$ distance ($r_{\text{sp}} = -0.41$ to 0.23) or formation distance ($r_{\text{sp}} = -0.58$ to 0.16),
- (xii) the maximum gas mass within R_{vir} over cosmic time ($r_{\text{sp}} = -0.21$ to 0.44),
- (xiii) the mean stellar age ($r_{\text{sp}} = -0.46$ to 0.23).

The final point appears contradictory to the picture that we describe above at first glance: if discs form late, then one would naively expect the mean stellar age, or a_*^{50} , to correlate with morphology. However, by close inspection of Fig. 1 (and as we will show further in Section 5), one can see that while the disc of a given galaxy is (almost) always younger than the bulge of that galaxy, discs emerge at different times in different galaxies. For example, the disc of Romeo is composed of stars with an average age of ~ 6 Gyr, while m12f, which hosts a disc and a bulge, formed its disc much more recently.

5 THE EVOLUTION OF THE STELLAR MORPHOLOGY

5.1 Overview

As the previous section showed, the $z = 0$ morphology is driven primarily by a combination of the accretion histories, the degree of rotation support in the halo at the half-mass time of the galaxy, and the relative amount of mass and angular momentum from the halo that end up in the disc. However, the $z = 0$ morphology is also the culmination of star formation in the galaxy, stars being deposited onto the galaxy through mergers, and dynamical interactions altering the orbits of existing stars. In this section, we explore the birth morphologies of stars and the extent to which their orbits are shifted to lower circularities over time, and we demonstrate that while the $z = 0$ morphologies do correlate with the spin of the gas that they are born out of, the full picture depends on the mutual evolution of the gas kinematics and SFR, and the impact of dynamical heating on the galactic disc. We do not explicitly investigate the radial or vertical structure of the disc as a function of time, but we refer the reader to Ma et al. (2017b) for a detailed discussion of the evolution of the disc of m12i simulated with FIRE-1.

Fig. 11 shows, as a function of time, the instantaneous fraction of stars forming with circularities $|\varepsilon| \geq 0.5$ (measured at the time of formation) and with $\varepsilon \leq 0.5$, i.e. in a disc that is counter-rotating relative to the overall angular momentum axis of the existing stars in the galaxy, and the normalized SFR. We define the instantaneous birth disc fraction $f_{*,\text{birth}}^{\text{disc}}(t)$ from the first snapshot that each particle appears in, capturing the kinematics of stars that are at most ~ 20 Myr old. Circularities, and therefore disc fractions, are defined relative to the evolving \hat{z} -axis of the angular momenta of all the stars in the galaxy at a given time. The curves indicate running averages smoothed over ~ 300 Myr, but the qualitative conclusions are

insensitive to the size of this window. We count stars within $R_{90}^*(t)$, but we find similar results using all stars within a fixed cut of 30 physical kpc.

5.2 Most stars form in discy configurations

Fig. 11 illustrates several points about the evolution of the disc morphology. First, at late times, most stars forming in MW-mass galaxies (black curves) do so with disc-like kinematics. This does not preclude them from forming in bulges, however, since they can be compact, rotationally supported pseudo-bulge components. Even in our most bulge-dominated system ($f_{\text{disc}}^* \sim 0.2$), the ‘birth disc fraction’ is high at late times – only m12q does not have $f_{*,\text{birth}}^{\text{disc}} \sim 1$ at some point after $t \sim 10$ Gyr. The three galaxies with the lowest f_{disc}^* at $z = 0$ are also the only three to experience a significant fraction of counter-rotating star formation. In m12b, that star formation eventually builds enough of a disc to flip the overall angular momentum axis of the galaxy (which occurs at $t \sim 8$ Gyr when the cyan curve goes to zero), but in Batman and m12q it only decreases the $z = 0$ disc fraction by adding stars opposite to the predominant \hat{z} . Therefore, even though SFRs typically peak around $z \sim 1$, and dynamical interactions shift stars to lower circularity as time passes, MW-mass galaxies usually increase their disc fractions at late times through fresh star formation. Though it is not shown here, the disc size R_{90}^* also tends to grow smoothly after $z \sim 1$.

The remainder of the sample demonstrates that the interplay between the SFR and the fraction of stars forming in the disc as a function of time is also instrumental to the $z = 0$ morphology. During the very early of stages of their growth ($t \lesssim 2$ Gyr), the hosts are dwarf-size systems and experience chaotic, bursty star formation in clumpy, gas-rich dIrr-type progenitor galaxies. As the grey curves show, though, SFRs are typically relatively low at these early times. The transition to ordered star formation (which is strongly correlated with the emergence of an ordered gas disc; Ma et al. 2017b; Simons et al. 2017; Ceverino et al. 2017) occurs at different times and at a different rate in each system, but it often coincides with a peak in the star formation.

Both the timing of the transition and the behaviour of the SFR following it strongly influences the $z = 0$ morphology: galaxies with $f_{\text{disc}}^*(z = 0) \gtrsim 0.7$ shift to ordered star formation relatively early and maintain a relatively high SFR until $z = 0$. Lower f_{disc}^* galaxies either change over later (e.g. m12z) or have a relatively low SFR following the switch (e.g. Remus).

5.3 Disruption and disordering of stellar discs

Discs built by ordered star formation can also be heated and destroyed. Fig. 12 plots the disc fraction at $z = 0$ against both the cumulative fraction of stellar mass born in the galaxy with high ε and the maximum instantaneous fraction of stellar mass in the galaxy at any given time with high circularities. The scatter in $f_{*,\text{birth}}^{\text{disc}}$ is relatively small: all of the galaxies in our sample have $0.6 < f_{*,\text{birth}}^{\text{disc}} < 0.9$. Accounting for counter-rotating star formation, all of our systems form ≥ 75 per cent of their stars in a disc. In other words, most stars form in discy configurations, as argued above. Furthermore, counter-rotating young stars (which would be formed out of retrograde star-forming gas) are typically too rare to have a significant impact on the galaxy (Section 4.7). Though we do not show it here, we also note that the fraction of counter-rotating ($\varepsilon \leq -0.5$) stellar mass at $z = 0$ is extremely small in all but the most bulge-dominated systems. Moreover, while the maximum counter-rotating fraction at any given time is ~ 15 – 25 per cent across our

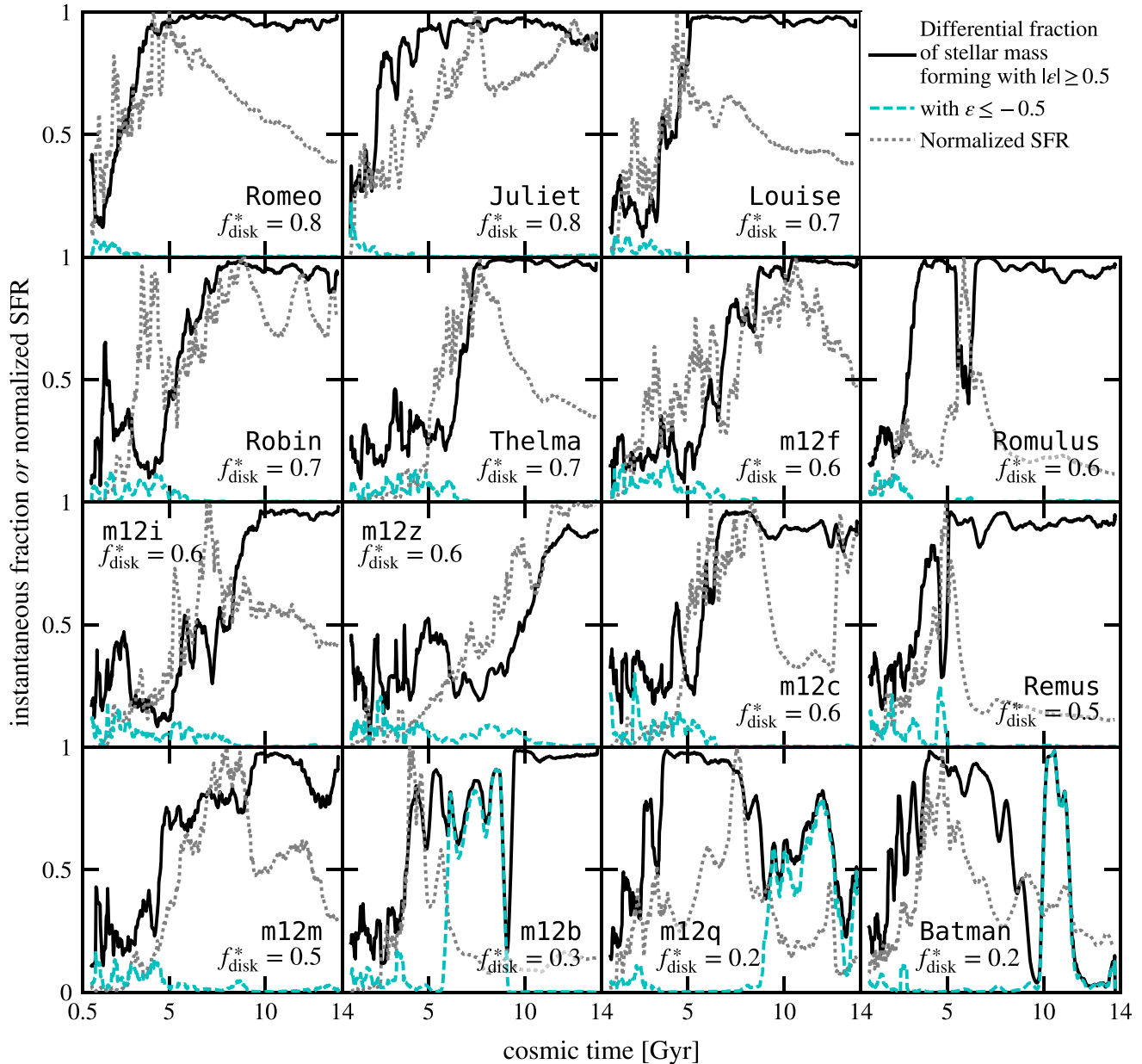


Figure 11. The instantaneous fraction of stars born in either a prograde or retrograde disc, i.e. with $|\varepsilon| \geq 0.5$ at formation (black); only in a counter-rotating disc, i.e. with $\varepsilon \leq -0.5$ at formation (dashed cyan); and the normalized SFR (grey dotted curves). Most stars with high circularity are formed at late times, though in *Batman* and *m12q* most of the young star formation occurs in a counter-rotating disc. The three galaxies with the lowest f_{disc}^* ($z = 0$) all experience some level of counter-rotating star formation; the remainder experience almost none. Galaxies with high $z = 0$ disc fractions have more prolonged disc-like star formation, but mergers sometimes destroy existing discs and scramble the correlation.

sample, these maxima occur at very early times ($z \gtrsim 3-4$) when the galaxies were at the dwarf mass scale. The exception is *m12b*, which builds a disc that is initially counter-rotating relative to the existing bulge but becomes large enough to dominate the angular momentum of the galaxy and flip the overall j_z vector; *m12b* therefore maximizes its counter-rotating fraction immediately before this transition at $z \sim 0.5$.

Because the galaxy masses and the degree of order in the galaxy build up over time, most of our galaxies have $f_{\text{disc}}^*(z = 0) \simeq \max[f_{\text{disc}}^*]$, i.e. the majority of our sample is at its ‘most disc-dominated’ today.

However, even bulge-dominated galaxies tended to have relatively strong discs at earlier times before having them destroyed by mergers and diluted by misaligned star formation. At $z \sim 1$, all of *Batman*, *m12q*, and *m12b* had discs that comprised 50–70 per cent of their stellar mass at that time. That is, while bulge-dominated systems arise from a combination of both nature and nurture, those in our sample were primarily differentiated from discy systems by the latter. Even though they do have more than twice as much retrograde star formation (relative to their total stellar mass) as any of the discier galaxies in our sample, the difference between their maximum f_{disc}^* and their $z = 0$ f_{disc}^* is much larger, indicating that

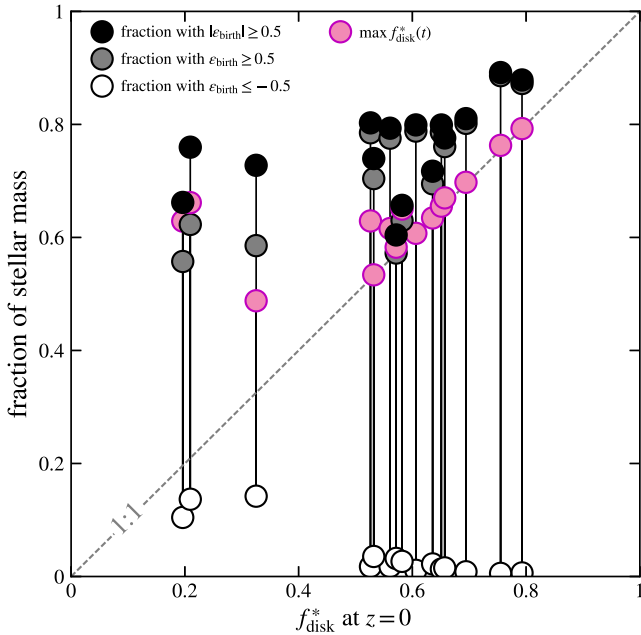


Figure 12. The cumulative fraction of stars born in a disc (i.e. with $|\varepsilon| \geq 0.5$, $\varepsilon \geq 0.5$, and $\varepsilon \leq -0.5$ at birth), and the maximum instantaneous fraction of the stellar mass in the galaxy at any given time with $\varepsilon \geq 0.5$ (i.e. $f_{\text{disc}}^*(t)$), all as a function of the disc fraction today. The fraction of stars born in counter-rotating discs (open black circles) is < 4 per cent in all but the most bulge-dominated galaxies. The spread in maximum disc fraction and in the birth disc fraction is surprisingly small (0.5–0.9): though $z = 0$ bulge-dominated systems do tend to form fewer stars with high $|\varepsilon|$ overall, and more stars in a counter-rotating disc, they are primarily differentiated by their subsequent evolution. Disc-dominated systems at $z = 0$ are more likely to be at or near their maximum disc fractions.

they were generally subject to more disc scrambling than the $z = 0$ disc-dominated galaxies.

Stars may also be shifted to lower circularities, while remaining on disc-like orbits, if the overall angular momentum axis of the galaxy shifts over time. Most of our sample is only marginally impacted by this effect: the angular momentum axis of our galaxies changes by $\lesssim 35^\circ$ after $z = 0.5$ in all but one of our galaxies. The exception, moreover, is m12b, which, as described above, builds a large enough young disc around the existing compact, bulgy core at late times to flip the overall angular momentum axis of the galaxy.

As discussed above, however, the $z = 0$ morphology is a very weak function of mean stellar age: the most bulge-dominated systems do tend to be the oldest, but the youngest systems are not necessarily disc-dominated. Thus, the length of time over which stellar orbits can be perturbed is not a primary driver of $z = 0$ morphology. In other words, while the bulge-dominated systems in our sample do have their pre-existing stellar discs destroyed by mergers or counter-rotating star formation, this can happen early or late in cosmic time.

6 GAS MORPHOLOGIES IN MW-MASS FIRE-2 GALAXIES

As reflected in Section 5 via the stellar circularities at birth, the star-forming gas in MW-mass galaxies is typically in a well-ordered disc with the majority of star formation occurring with $|\varepsilon| \gtrsim 0.75$. That is, regardless of the instantaneous state of the stars in the galaxy, the short dynamical memory of the gas leads to thin discs at nearly

all times in massive galaxies. For a detailed investigation of gas morphologies across a larger range of host masses in the FIRE-2 simulations, we refer the reader to El-Badry et al. (2018), who examined gas angular momentum and HI morphology as a function of galaxy mass from the dwarf scale to the MW scale, and showed that in dwarfs the degree of rotation support can be much lower.

6.1 MW-mass galaxies have rotationally supported gas discs

As demonstrated in Fig. 1, almost all of the gas in the galaxies is on circular, disc-like orbits at $z = 0$ (with the exception of m12q). Even without accounting for elliptical orbits, gas rotation curves are consistent with almost complete rotation support out to roughly R_{gas} in all the galaxies except Batman and m12q. In fact, with the exception of m12q, all of the galaxies have $f_{\text{gas}}^{\text{disc}} > 0.9$, with nine of the 15 exceeding 0.98. This is not particularly surprising at these masses, where pressure support for $T \lesssim 10^4$ K gas is very weak.

6.2 Visual morphologies of gas discs

Fig. 13 shows face-on and edge-on projections of the gas in the FIRE-2 galaxies, again sorted by increasing f_{disc}^* . As in Fig. 2, the circles and rectangles indicate R_{gas} and Z_{gas} . Even with (almost) all of the galaxies having $f_{\text{gas}}^{\text{disc}} > 0.9$, there exists some diversity in the shape of the discs, and even more diversity in the radial extent. For example, m12f very recently interacted with a gas-rich subhalo, leaving a marginally disturbed gas disc at $z = 0$. m12q has effectively no gas remaining at $z = 0$, having consumed the last of its gas disc at $z \sim 0.1$. Batman has a clear warp near the centre of the disc, likely created because the $z = 0$ gas disc is formed out of an ongoing accretion event. Romulus and Louise display similar warps near the edges of their discs. Batman is also the only galaxy with a gas disc misaligned from the stellar disc by more than 4° . This misalignment presumably survives because the gas is being continually replenished at $z \sim 0$ (van de Voort et al. 2015), and likely also because Batman has a relatively spherical stellar distribution: the ratio of the shortest to longest principal axes, (c/a) , of the stars within 10 kpc is 0.72.¹⁷

6.3 Sizes of gas discs

Fig. 14 explores the radial extent of the gas discs. The radius of the gas disc is closely tied to the amount of gas in the galaxy, in broad agreement with the observed relationship between the size of gas discs and the amount of gas in those discs (e.g. Wang et al. 2016), and potentially in agreement with arguments based on the Toomre (1964) stability parameter (Schmitz et al., in preparation).

R_{gas} is also correlated with the morphology of the stellar component: the points in Fig. 14 are coloured by f_{disc}^* and are generally correlated with R_{90}^* , though the gas discs are typically more extended. To the extent that this is causal, it appears primarily to owe to the fact that higher late-time gas masses are associated both with larger R_{gas} and discier galaxies.

Though our sample size is small, and we have yet to identify any underlying physical drivers, we note galaxies in our paired sample tend to have higher R_{gas} overall. This is apparent even by eye in Fig. 13: the numbers in parentheses, which indicate the rank of R_{gas} for each galaxy, show that the five largest gas discs are all in haloes that reside in a Local Group-like environment. However, with such a small sample size, it is impossible to reject the null hypothesis that

¹⁷The remainder of the sample all have $(c/a)_{*} (< 10 \text{ kpc}) \lesssim 0.5$.

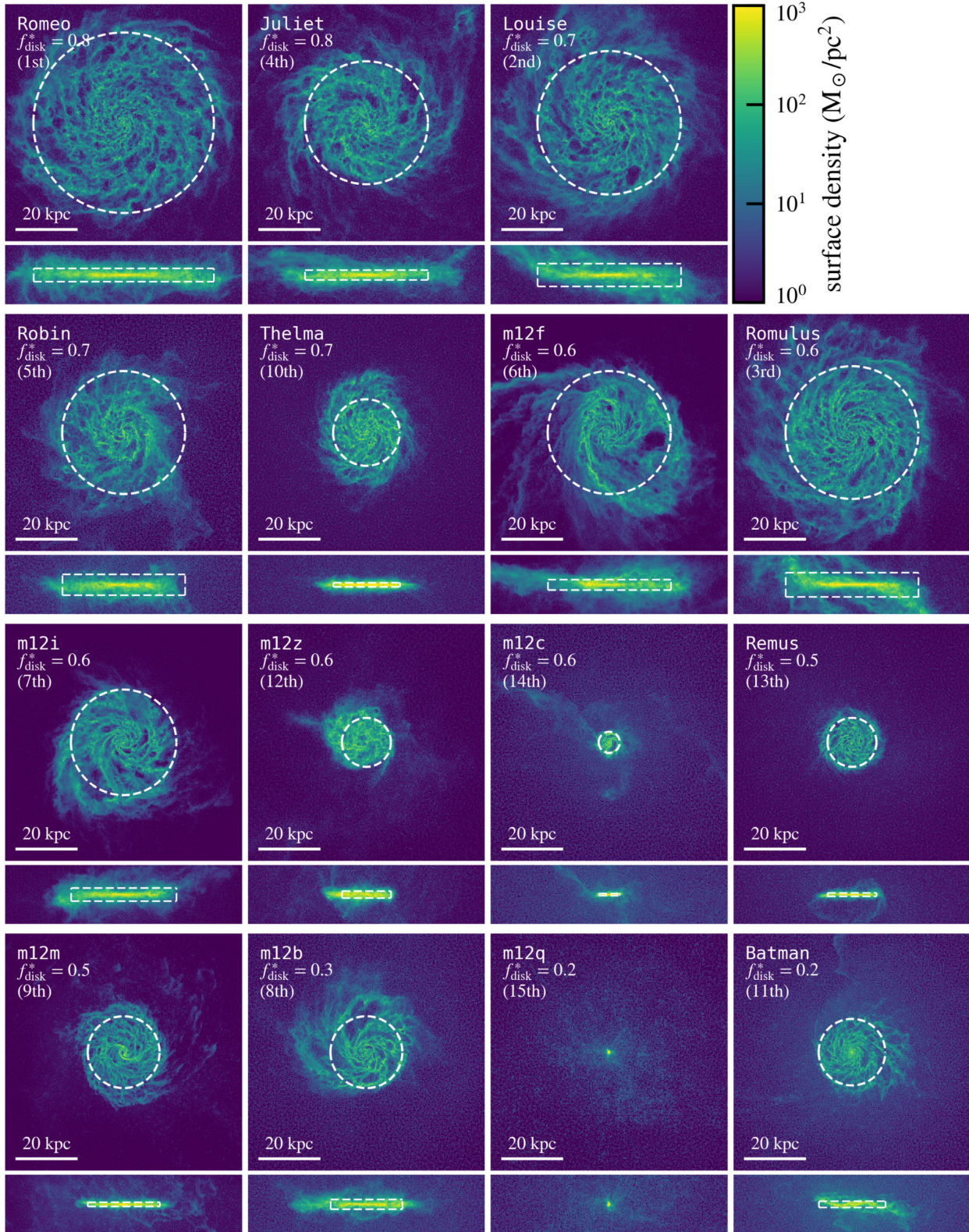


Figure 13. Gas column density maps of the galaxies in our sample. Galaxies are again sorted by decreasing f_{disc}^* , but the number in parentheses indicates the rank (from largest to smallest) that each galaxy has when sorted by R_{gas} . Batman has a significant $\sim 20^\circ$ warp, likely induced because the $z = 0$ gas disc is built from an ongoing merger that is misaligned with the stars, and m12q exhausted most of its gas supply at $z \sim 0.1$; the remainder of the MW-mass FIRE-2 galaxies have thin, rotation supported discs ($f_{\text{gas}}^{\text{disc}} \geq 0.9$) at $z = 0$. We therefore focus on the size of the gas disc, rather than the corotation fraction. The dashed lines indicate the adopted radial and vertical extents of the gas discs; they are not shown for m12q where they are < 1 kpc.

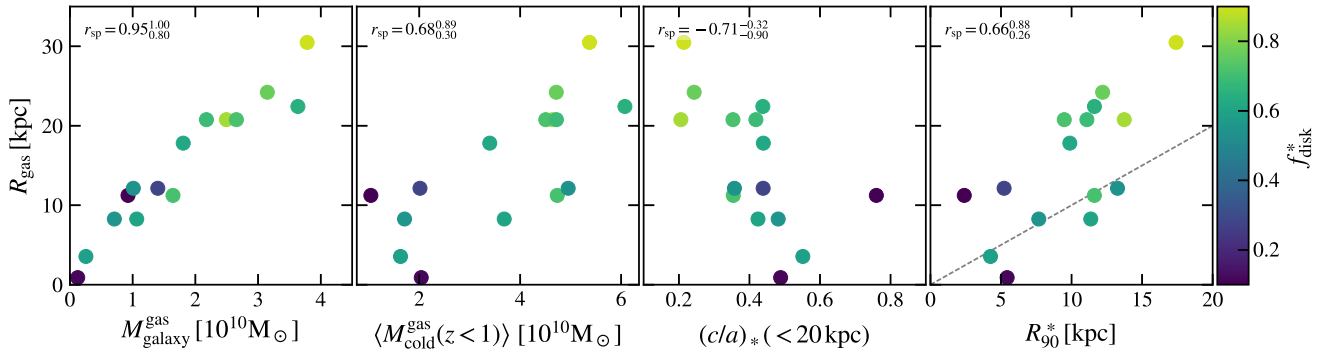


Figure 14. The size of the gas discs R_{gas} versus the gas mass within R_{gas} and Z_{gas} , $M_{\text{galaxy}}^{\text{gas}}$; the average mass in $T < 10^5$ K gas within the virial radius after $z = 1$, $\langle M_{\text{cold}}^{\text{gas}}(z < 1) \rangle$; the ratio of the shortest to longest principal axes of the stars within 20 kpc, $(c/a)_* (< 20 \text{ kpc})$; and the radial extent of the stars, R_{90}^* . The dashed grey line in the final column is one-to-one, indicating that the majority of the gas discs extend well beyond the stellar discs. The points are coloured by f_{disc}^* , which also correlates reasonably strongly with R_{gas} .

they are drawn from the same distribution and, without tying R_{gas} to a property of the DMO halo, we cannot directly test this hypothesis with a larger sample. Neither R_{gas} nor the residuals about a power-law fit of $R_{\text{gas}}(M_{\text{galaxy}}^{\text{gas}})$ strongly correlate with any of the DMO halo properties that we have checked, including the $z = 0$ spin of the DMO halo ($r_{\text{sp}} = -0.21$ to 0.79). We have also tested whether the Fall (1983) and Mo et al. (1998) model accurately predicts the sizes of gas discs at $z = 0$ based on the DMO halo, and find relatively poor correlations between the model predictions and the actual radial extents ($r_{\text{sp}} = -0.05$ to 0.79 for the isothermal potential and $r_{\text{sp}} = -0.26$ to 0.69 for the NFW model).

7 CONCLUSIONS

In this work, we examined the kinematics and morphologies of MW-mass galaxies ($10^{10.5} \lesssim M_{\text{galaxy}}^*/M_{\odot} \lesssim 10^{11.5}$) simulated with the FIRE-2 physics. Our sample includes 15 galaxies with effective stellar radii ranging from ~ 1 to 17 kpc, and kinematic disc fractions varying from ~ 0.2 to 0.8 . We first demonstrated that these morphological measures broadly correlate with each other (though there is appreciable scatter), and that both also correlate with a variety of other morphological measures. In particular, Σ_1 is a reasonably accurate descriptor of the overall morphology over this narrow mass range at $z = 0$.

We then showed that the Fall (1983) model, wherein the baryons that form the disc are assumed to have the same specific angular momentum of their host DM haloes, produces an estimate for galaxy sizes (and how they correlate with mass over a large dynamic range) that is accurate at the order-of-magnitude level, but fails to recover the actual half-mass radii of our galaxies. This is due primarily to the scatter in the amount of specific angular momentum that each galaxy acquires: j_d/m_d has nearly an order of magnitude spread overall. Moreover, there are no obvious trends between the morphology of a galaxy and either the mass accretion history or the merger history of the host halo in the DMO simulation: both our most bulge-dominated and our most disc-dominated galaxies experience their last major merger at $z \sim 2-3$. It therefore remains difficult to predict the morphology of a galaxy that would form in a given halo based purely on the information available from a DMO simulation.

Instead, accurate predictors of morphology within this narrow mass range are related to the gas accretion and galaxy merger histories. Systems that maintain high gas fractions to late times tend to

be disc-dominated at $z = 0$ (generally growing inside-out, with R_{90}^* increasing over time), while those that maximize their star-forming reservoir early tend to be bulge-dominated at $z = 0$. Based primarily on visual inspection of the movies, the amount of gas in the galaxy over time appears to be driven by a combination of the impact parameter and timing of galactic mergers, along with the amount of gas in the halo that cools and accretes onto the galaxy at late times. We reiterate that our results apply only at this specific mass, however: lower mass galaxies that cannot maintain an ordered gas disc at late times (e.g. El-Badry et al. 2018) would not necessarily follow the trends identified here.

We find good correlations between morphology and the spin of the gas in the halo when the galaxy had formed half of its $z = 0$ stellar mass, along with the average amount of gas available to form stars at late times. These quantities also correlate (though less strongly) with one another: gas that infalls at later times tends to have more angular momentum. However, we find no clear route from the host properties available only from a DMO simulation to galactic morphology: neither the DMO mass accretion history, the half-mass formation time of the halo nor the spin of the DM at the halo half-mass formation time (either in the hydrodynamic or DMO simulation) correlate significantly with morphology, emphasizing the difficulty of using DMO simulations to predict morphology. None the less, our analysis does not preclude a multivariate relationship between morphology and DMO properties. In fact, given the correlation between λ_{DMO} at a_*^{50} and the morphology at $z = 0$, there are hints that such a relationship may exist, but we lack the sample size to test for those.

The prediction that the spin of the gas in the halo at the stellar half-mass formation time (i.e. the angular momentum support of the gas that contributes to building the galaxy) drives the late-time morphologies of MW-mass galaxies may eventually be observationally falsifiable. Wide-field observations with integral field spectroscopy (e.g. with instruments similar to the Keck Cosmic Web Imager; Morrissey & KCWI Team 2013) could potentially map out the angular momentum in the cold CGM gas and ultimately measure the distribution of that angular momentum across haloes. If the picture laid out here is correct, then the shapes of that distribution and the distribution of the morphologies of $z = 0$ MW-mass galaxies should broadly agree.

The $z = 0$ morphologies can also be viewed as the summation of a Hubble time of star formation and subsequent heating of those

stars (either from mergers, e.g. Toomre & Toomre 1972; Hernquist 1992; Quinn, Hernquist & Fullagar 1993; Sanders & Mirabel 1996, or from internal interactions, e.g. Minchev & Quillen 2006; Saha, Tseng & Taam 2010). We showed that most stars in MW-mass galaxies formed from gas that was discy at the time of star formation (i.e. with circularity $|\epsilon| \geq 0.5$). The most bulge-dominated galaxies at $z = 0$ tend to have the lowest fraction of stars born in a prograde disc (and the highest fraction born in a retrograde one), but they also show the largest differences between their birth and $z = 0$ kinematics. Therefore, while dispersion supported galaxies arise from a combination of birth stellar kinematics and subsequent stellar heating that destroys ordered rotation, our results suggest the latter effect is far more important.

At late times ($z \lesssim 1 - 2$), nearly all of the stars born in MW-mass galaxies have disc-like kinematics, such that f_{disc}^* always grows after $z \sim 1$. We do see two exceptions, which actually lower their disc fractions (slightly) at $z \lesssim 0.5$ by forming stars in a counter-rotating disc, but this is only possible because those galaxies are already dispersion supported when cold gas is added to the central galaxy at low redshift. Moreover, we emphasize that the counter-rotating discs do not *determine* the bulginess of the galaxy. We do not expect ‘clump sinking’ to play a significant role in bulge formation for systems that are MW mass at $z = 0$ (whose progenitors were dwarfs at high redshift).

The gas in the MW-mass FIRE-2 galaxies, meanwhile, always settles into a largely rotation-supported disc at late times. All but one of our galaxies maintain that disc to $z = 0$, either through fresh accretion from merging satellites or condensation out of the CGM. The size of the gas disc is primarily driven by its mass.

Our results generally agree with the results of some previous work on the formation of galactic discs in hydrodynamic simulations of MW-mass galaxies, which have found that star formation is chaotic and bursty at high redshift, with well-ordered gas discs only appearing after $z \sim 1$ for galaxies with MW masses at $z = 0$ (for more-/less-massive galaxies, the transition occurs earlier/later; see Muratov et al. 2015; Feldmann & Mayer 2015; Simons et al. 2017; Hayward & Hopkins 2017; Sparre et al. 2017; Faucher-Giguère 2018.) The supply of the gas available to form that disc, therefore, determines the amount of stars that form with tangential orbits relative to radial orbits. In agreement with several authors (e.g. Scannapieco et al. 2009; Sales et al. 2012; Rodriguez-Gomez et al. 2017), we find no strong morphological trends with the $z = 0$ spin of the DM halo at the MW-mass scale.

While our qualitative results are robust to the mass resolution of the simulations (Appendix A), the quantitative morphology of a given galaxy does change slightly with resolution. However, these changes can typically be understood in terms of the trends that we identify here (e.g. because a slightly different merger history arises at different resolutions). We also caution that half of our sample is in Local Group-like pairs. While these are more directly comparable to the MW and Andromeda galaxies than simulations of isolated MW-mass hosts, there may be environmental effects that bias our results. However, because these effects should enter via properties of the halo or galaxy, such as the halo spin or mass accretion history, our analysis will automatically include any changes caused by the 1 Mpc environment.

This work has investigated potential relationships between theoretical measures of morphology and (potentially unobservable) physical properties of the simulated galaxies in an attempt to understand the physical driver(s) of morphology in the simulations, not to compare with observations. We plan to probe the relationship

between theoretical morphological measures of the FIRE-2 galaxies, like those presented here, and estimates extracted from mock observations, including the kinematic distributions (e.g. Zhu et al. 2018), in future work.

ACKNOWLEDGEMENTS

The authors thank Astrid Lamberts, Coral Wheeler, Evan Kirby, Laura Sales, and Virginia Kilborn for valuable discussions, and the anonymous referee for their helpful comments. We also thank the Santa Cruz Galaxy Formation Workshop, the Galaxy Formation and Evolution in Southern California (GalFRESCA) workshop, and the Swinburne-Caltech workshop for spawning useful discussions that significantly improved the quality of the manuscript, and we thank Alexander Knebe, Peter Behroozi, and Oliver Hahn, respectively, for making *AHF*, *rockstar* and *consistent-trees*, and *MUSIC* publicly available.

Support for SGK was provided by NASA through Einstein Postdoctoral Fellowship grant number PF5-160136 awarded by the Chandra X-ray Center, which is operated by the Smithsonian Astrophysical Observatory for NASA under contract NAS8-03060. Support for PFH was provided by an Alfred P. Sloan Research Fellowship, NSF Collaborative Research grant no. 1715847 and CAREER grant no. 1455342. AW was supported by a Caltech-Carnegie Fellowship, in part through the Moore Center for Theoretical Cosmology and Physics at Caltech, and by NASA through grants HST-GO-14734 and HST-AR-15057 from STScI. RES is supported by an NSF Astronomy and Astrophysics Postdoctoral Fellowship under grant AST-1400989. KEB was supported by a Berkeley graduate fellowship, a Hellman award for graduate study, and an NSF Graduate Research Fellowship. EQ was supported in part by NSF grant AST-1715070 and a Simons Investigator Award from the Simons Foundation. JSB was supported by NSF grant AST-1518291 and by NASA through *Hubble Space Telescope* theory grants (programs AR-13921, AR-13888, and AR-14282.001) awarded by STScI, which is operated by the Association of Universities for Research in Astronomy (AURA), Inc., under NASA contract NAS5-26555. ZH and CAFG were supported by NSF through grants AST-1412836, AST-1517491, AST-1715216, and CAREER award AST-1652522, and by NASA through grant NNX15AB22G, and ZH additionally acknowledges support from support from Northwestern University through the ‘Reach for the Stars’ program. FvdV acknowledges support from the Klaus Tschira Foundation. The Flatiron Institute is supported by the Simons Foundation. DK acknowledges support from NSF grant AST-1412153, NSF grant AST-1715101, and the Cottrell Scholar Award from the Research Corporation for Science Advancement. MBK acknowledges support from NSF grant AST-1517226 and from NASA grants NNX17AG29G and HST-AR-13896, HST-AR-14282, HST-AR-14554, HST-GO-12914, and HST-GO-14191 from STScI.

Numerical calculations were run on the Caltech compute cluster ‘Wheeler,’ allocations from XSEDE TG-AST130039 and PRAC NSF.1713353 supported by the NSF, NASA HEC SMD-16-7223, and SMD-16-7592, and High Performance Computing at Los Alamos National Labs. This work also made use of *ASTROPY*, a community-developed core PYTHON package for Astronomy (Astropy Collaboration et al. 2013), *MATPLOTLIB* (Hunter 2007), *NUMPY* (van der Walt, Colbert & Varoquaux 2011), *SCIPY* (Jones et al. 2001), *IPYTHON* (Perez & Granger 2007), and NASA’s Astrophysics Data System.

REFERENCES

- Abadi M. G., Navarro J. F., Steinmetz M., Eke V. R., 2003, *ApJ*, 597, 21
- Agertz O., Kravtsov A. V., 2016, *ApJ*, 824, 79
- Agertz O., Teyssier R., Moore B., 2011, *MNRAS*, 410, 1391
- Anglés-Alcázar D., Davé R., Özel F., Oppenheimer B. D., 2014, *ApJ*, 782, 84
- Anglés-Alcázar D., Faucher-Giguère C.-A., Kereš D., Hopkins P. F., Quataert E., Murray N., 2017, *MNRAS*, 470, 4698
- Astropy Collaboration et al., 2013, *A&A*, 558, A33
- Aumer M., White S. D. M., Naab T., Scannapieco C., 2013, *MNRAS*, 434, 3142
- Bailin J., Steinmetz M., 2005, *ApJ*, 627, 647
- Bamford S. P. et al., 2009, *MNRAS*, 393, 1324
- Barnes J. E., Hernquist L. E., 1991, *ApJ*, 370, L65
- Behroozi P. S., Wechsler R. H., Wu H.-Y., 2013a, *ApJ*, 762, 109
- Behroozi P. S., Wechsler R. H., Wu H.-Y., Busha M. T., Klypin A. A., Primack J. R., 2013b, *ApJ*, 763, 18
- Behroozi P. S., Wechsler R. H., Conroy C., 2013c, *ApJ*, 770, 57
- Bell E. F. et al., 2012, *ApJ*, 753, 167
- Bett P., Eke V., Frenk C. S., Jenkins A., Okamoto T., 2010, *MNRAS*, 404, 1137
- Bournaud F. et al., 2011, *ApJ*, 730, 4
- Bower R. G., Benson A. J., Malbon R., Helly J. C., Frenk C. S., Baugh C. M., Cole S., Lacey C. G., 2006, *MNRAS*, 370, 645
- Brooks A., Christensen C., 2016, *Galactic Bulges*, 418, 317
- Bryan G. L., Norman M. L., 1998, *ApJ*, 495, 80
- Bullock J. S., Kravtsov A. V., Weinberg D. H., 2001, *ApJ*, 548, 33
- Cattaneo A., Dekel A., Devriendt J., Guiderdoni B., Blaizot J., 2006, *MNRAS*, 370, 1651
- Ceverino D., Primack J., Dekel A., Kassir S. A., 2017, *MNRAS*, 467, 2664
- Chan T. K., Kereš D., Oñorbe J., Hopkins P. F., Muratov A. L., Faucher-Giguère C.-A., Quataert E., 2015, *MNRAS*, 454, 2981
- Cheung E. et al., 2012, *ApJ*, 760, 131
- Colín P., Avila-Reese V., Roca-Fàbrega S., Valenzuela O., 2016, *ApJ*, 829, 98
- Crain R. A. et al., 2009, *MNRAS*, 399, 1773
- Croton D. J. et al., 2006, *MNRAS*, 365, 11
- Debatista V. P., Gonzalez O. A., Sanderson R. E., El-Badry K., Garrison-Kimmel S., Wetzel A., Faucher-Giguère C.-A., Hopkins P. F., 2018, preprint ([arXiv:1805.12199](https://arxiv.org/abs/1805.12199))
- El-Badry K., Wetzel A., Geha M., Hopkins P. F., Kereš D., Chan T. K., Faucher-Giguère C.-A., 2016, *ApJ*, 820, 131
- El-Badry K. et al., 2018, *MNRAS*, 473, 1930
- Escala I. et al., 2018, *MNRAS*, 474, 2194
- Fall S. M., 1983, in Athanassoula E., ed., *IAU Symp. Vol. 100, Internal Kinematics and Dynamics of Galaxies*. Kluwer, Dordrecht, p. 391
- Fall S. M., Efstathiou G., 1980, *MNRAS*, 193, 189
- Fall S. M., Romanowsky A. J., 2013, *ApJ*, 769, L26
- Fang J. J., Faber S. M., Koo D. C., Dekel A., 2013, *ApJ*, 776, 63
- Faucher-Giguère C.-A., 2018, *MNRAS*, 473, 3717
- Faucher-Giguère C.-A., Lidz A., Zaldarriaga M., Hernquist L., 2009, *ApJ*, 703, 1416
- Feldmann R., Mayer L., 2015, *MNRAS*, 446, 1939
- Fiacconi D., Feldmann R., Mayer L., 2015, *MNRAS*, 446, 1957
- Förster Schreiber N. M. et al., 2011, *ApJ*, 739, 45
- Garrison-Kimmel S., Boylan-Kolchin M., Bullock J. S., Lee K., 2014, *MNRAS*, 438, 2578
- Garrison-Kimmel S. et al., 2017, *MNRAS*, 471, 1709
- Genel S., Fall S. M., Hernquist L., Vogelsberger M., Snyder G. F., Rodriguez-Gomez V., Sijacki D., Springel V., 2015, *ApJ*, 804, L40
- Genel S. et al., 2018, *MNRAS*, 474, 3976
- Governato F., Willman B., Mayer L., Brooks A., Stinson G., Valenzuela O., Wadsley J., Quinn T., 2007, *MNRAS*, 374, 1479
- Governato F. et al., 2009, *MNRAS*, 398, 312
- Grand R. J. J. et al., 2017, *MNRAS*, 467, 179
- Guedes J., Callegari S., Madau P., Mayer L., 2011, *ApJ*, 742, 76
- Hafen Z. et al., 2017, *MNRAS*, 469, 2292
- Hayward C. C., Hopkins P. F., 2017, *MNRAS*, 465, 1682
- Hernquist L., 1992, *ApJ*, 400, 460
- Hopkins P. F., 2015, *MNRAS*, 450, 53
- Hopkins P. F., 2017, *MNRAS*, 466, 3387
- Hopkins P. F. et al., 2009a, *MNRAS*, 397, 802
- Hopkins P. F., Cox T. J., Younger J. D., Hernquist L., 2009b, *ApJ*, 691, 1168
- Hopkins P. F. et al., 2010, *ApJ*, 715, 202
- Hopkins P. F., Narayanan D., Murray N., 2013, *MNRAS*, 432, 2647
- Hopkins P. F., Kereš D., Oñorbe J., Faucher-Giguère C.-A., Quataert E., Murray N., Bullock J. S., 2014, *MNRAS*, 445, 581
- Hopkins P. F. et al., 2018, *MNRAS*, 480, 800
- Howes L. M. et al., 2015, *Nature*, 527, 484
- Hubble E. P., 1926, *ApJ*, 64, 321
- Huertas-Company M., Aguerri J. A. L., Bernardi M., Mei S., Sánchez Almeida J., 2011, *A&A*, 525, A157
- Hunter J. D., 2007, *Comput. Sci. Eng.*, 9, 90
- Jones E. et al., 2001, *SciPy: open source scientific tools for Python*. Available at: <http://www.scipy.org/>, (Accessed October 25, 2017)
- Katz N., White S. D. M., 1993, *ApJ*, 412, 455
- Kaufmann T., Wheeler C., Bullock J. S., 2007, *MNRAS*, 382, 1187
- Kepner J. V., 1999, *ApJ*, 520, 59
- Kereš D., Hernquist L., 2009, *ApJ*, 700, L1
- Kereš D., Katz N., Weinberg D. H., Davé R., 2005, *MNRAS*, 363, 2
- Kravtsov A. V., 2013, *ApJ*, 764, L31
- Kroupa P., 2001, *MNRAS*, 322, 231
- Krumholz M. R., Gnedin N. Y., 2011, *ApJ*, 729, 36
- Lagos C. d. P., Theuns T., Stevens A. R. H., Cortese L., Padilla N. D., Davis T. A., Contreras S., Croton D., 2017, *MNRAS*, 464, 3850
- Larson D. et al., 2011, *ApJS*, 192, 16
- Leitherer C. et al., 1999, *ApJS*, 123, 3
- Ludlow A. D., Navarro J. F., Angulo R. E., Boylan-Kolchin M., Springel V., Frenk C., White S. D. M., 2014, *MNRAS*, 441, 378
- Ma X., Hopkins P. F., Faucher-Giguère C.-A., Zolman N., Muratov A. L., Kereš D., Quataert E., 2016, *MNRAS*, 456, 2140
- Ma X., Hopkins P. F., Feldmann R., Torrey P., Faucher-Giguère C.-A., Kereš D., 2017a, *MNRAS*, 466, 4780
- Ma X., Hopkins P. F., Wetzel A. R., Kirby E. N., Anglés-Alcázar D., Faucher-Giguère C.-A., Kereš D., Quataert E., 2017b, *MNRAS*, 467, 2430
- Mandelker N., Dekel A., Ceverino D., DeGraf C., Guo Y., Primack J., 2017, *MNRAS*, 464, 635
- Marinacci F., Pakmor R., Springel V., 2014, *MNRAS*, 437, 1750
- Merritt A., van Dokkum P., Abraham R., Zhang J., 2016, *ApJ*, 830, 62
- Minchev I., Quillen A. C., 2006, *MNRAS*, 368, 623
- Mo H. J., Mao S., White S. D. M., 1998, *MNRAS*, 295, 319
- Morrissey P. KCWI Team, 2013, *American Astronomical Society Meeting Abstracts*, #221, p. 345.05
- Murante G., Monaco P., Borgani S., Tornatore L., Dolag K., Goz D., 2015, *MNRAS*, 447, 178
- Muratov A. L., Kereš D., Faucher-Giguère C.-A., Hopkins P. F., Quataert E., Murray N., 2015, *MNRAS*, 454, 2691
- Navarro J. F., Frenk C. S., White S. D. M., 1996, *ApJ*, 462, 563
- Okamoto T., Eke V. R., Frenk C. S., Jenkins A., 2005, *MNRAS*, 363, 1299
- Oklopčić A., Hopkins P. F., Feldmann R., Kereš D., Faucher-Giguère C.-A., Murray N., 2017, *MNRAS*, 465, 952
- Oñorbe J., Garrison-Kimmel S., Maller A. H., Bullock J. S., Rocha M., Hahn O., 2014, *MNRAS*, 437, 1894
- Orr M. E. et al., 2018, *MNRAS*, 478, 3653
- Pedrosa S. E., Tissera P. B., 2015, *A&A*, 584, A43
- Pedrosa S. E., Tissera P. B., De Rossi M. E., 2014, *A&A*, 567, A47
- Peebles P. J. E., 1969, *ApJ*, 155, 393
- Peirani S., Mohayaee R., de Freitas Pacheco J. A., 2004, *MNRAS*, 348, 921
- Perez F., Granger B. E., 2007, *Comput. Sci. Eng.*, 9, 21
- Pichon C., Pogosyan D., Kimm T., Slyz A., Devriendt J., Dubois Y., 2011, *MNRAS*, 418, 2493
- Pilkington K. et al., 2012, *A&A*, 540, A56
- Pillepich A. et al., 2018, *MNRAS*, 473, 4077
- Planck Collaboration et al., 2016, *A&A*, 594, A13
- Pontzen A., Governato F., 2012, *MNRAS*, 421, 3464

- Posti L., Pezzulli G., Fraternali F., Di Teodoro E. M., 2018, *MNRAS*, 475, 232
- Power C., Navarro J. F., Jenkins A., Frenk C. S., White S. D. M., Springel V., Stadel J., Quinn T., 2003, *MNRAS*, 338, 14
- Price D. J., Monaghan J. J., 2007, *MNRAS*, 374, 1347
- Quinn P. J., Hernquist L., Fullagar D. P., 1993, *ApJ*, 403, 74
- Robertson B. E., Bullock J. S., 2008, *ApJ*, 685, L27
- Robertson B., Bullock J. S., Cox T. J., Di Matteo T., Hernquist L., Springel V., Yoshida N., 2006, *ApJ*, 645, 986
- Rodríguez-Gomez V. et al., 2017, *MNRAS*, 467, 3083
- Rodríguez-Puebla A., Primack J. R., Avila-Reese V., Faber S. M., 2017, *MNRAS*, 470, 651
- Romanowsky A. J., Fall S. M., 2012, *ApJS*, 203, 17
- Roškar R., Teysier R., Agertz O., Wetzstein M., Moore B., 2014, *MNRAS*, 444, 2837
- Saha K., Tseng Y.-H., Taam R. E., 2010, *ApJ*, 721, 1878
- Sales L. V., Navarro J. F., Theuns T., Schaye J., White S. D. M., Frenk C. S., Crain R. A., Dalla Vecchia C., 2012, *MNRAS*, 423, 1544
- Salim S. et al., 2007, *ApJS*, 173, 267
- Sanders D. B., Mirabel I. F., 1996, *ARA&A*, 34, 749
- Sanderson R. E. et al., 2017, preprint ([arXiv:1712.05808](https://arxiv.org/abs/1712.05808))
- Scannapieco C., Tissera P. B., White S. D. M., Springel V., 2008, *MNRAS*, 389, 1137
- Scannapieco C., White S. D. M., Springel V., Tissera P. B., 2009, *MNRAS*, 396, 696
- Scannapieco C., Gadotti D. A., Jonsson P., White S. D. M., 2010, *MNRAS*, 407, L41
- Schaye J. et al., 2015, *MNRAS*, 446, 521
- Sérsic J. L., 1963, *Bol. Asoc. Argentina Astron. La Plata Argentina*, 6, 41
- Shen S., Mo H. J., White S. D. M., Blanton M. R., Kauffmann G., Voges W., Brinkmann J., Csabai I., 2003, *MNRAS*, 343, 978
- Simons R. C., Kassin S. A., Weiner B. J., Heckman T. M., Lee J. C., Lotz J. M., Peth M., Tchernyshyov K., 2015, *MNRAS*, 452, 386
- Simons R. C. et al., 2017, *ApJ*, 843, 46
- Sokolowska A., Capelo P. R., Fall S. M., Mayer L., Shen S., Bonoli S., 2017, *ApJ*, 835, 289
- Somerville R. S., Hopkins P. F., Cox T. J., Robertson B. E., Hernquist L., 2008, *MNRAS*, 391, 481
- Sparre M., Hayward C. C., Feldmann R., Faucher-Giguère C.-A., Muratov A. L., Kereš D., Hopkins P. F., 2017, *MNRAS*, 466, 88
- Springel V., 2005, *MNRAS*, 364, 1105
- Springel V., Hernquist L., 2005, *ApJ*, 622, L9
- Springel V. et al., 2005, *Nature*, 435, 629
- Stewart K. R., Bullock J. S., Wechsler R. H., Maller A. H., 2009, *ApJ*, 702, 307
- Stewart K. R., Kaufmann T., Bullock J. S., Barton E. J., Maller A. H., Diemand J., Wadsley J., 2011, *ApJ*, 738, 39
- Stewart K. R., Brooks A. M., Bullock J. S., Maller A. H., Diemand J., Wadsley J., Moustakas L. A., 2013, *ApJ*, 769, 74
- Stewart K. R. et al., 2017, *ApJ*, 843, 47
- Stinson G. S. et al., 2012, *MNRAS*, 425, 1270
- Su K.-Y., Hopkins P. F., Hayward C. C., Faucher-Giguère C.-A., Kereš D., Ma X., Robles V. H., 2017, *MNRAS*, 471, 144
- Teklu A. F., Remus R.-S., Dolag K., Beck A. M., Burkert A., Schmidt A. S., Schulze F., Steinborn L. K., 2015, *ApJ*, 812, 29
- Toomre A., 1964, *ApJ*, 139, 1217
- Toomre A., Toomre J., 1972, *ApJ*, 178, 623
- van de Voort F., Davis T. A., Kereš D., Quataert E., Faucher-Giguère C.-A., Hopkins P. F., 2015, *MNRAS*, 451, 3269
- van der Walt S., Colbert S. C., Varoquaux G., 2011, *Comput. Sci. Eng.*, 13, 22
- van Dokkum P. G., 2005, *AJ*, 130, 2647
- van Dokkum P. G. et al., 2010, *ApJ*, 709, 1018
- Vogelsberger M. et al., 2014a, *MNRAS*, 444, 1518
- Vogelsberger M. et al., 2014b, *Nature*, 509, 177
- Wang L., Dutton A. A., Stinson G. S., Macciò A. V., Penzo C., Kang X., Keller B. W., Wadsley J., 2015, *MNRAS*, 454, 83
- Wang J., Koribalski B. S., Serra P., van der Hulst T., Roychowdhury S., Kamphuis P., N. Chengalur J., 2016, *MNRAS*, 460, 2143
- Weinberger R. et al., 2017, *MNRAS*, 465, 3291
- Wetzel A. R., Hopkins P. F., Kim J.-h., Faucher-Giguère C.-A., Kereš D., Quataert E., 2016, *ApJ*, 827, L23
- Wheeler C. et al., 2017, *MNRAS*, 465, 2420
- White S. D. M., 1984, *ApJ*, 286, 38
- White S. D. M., Rees M. J., 1978, *MNRAS*, 183, 341
- Woo J. et al., 2013, *MNRAS*, 428, 3306
- Woo J., Dekel A., Faber S. M., Koo D. C., 2015, *MNRAS*, 448, 237
- Woo J., Carollo C. M., Faber S. M., Dekel A., Tacchella S., 2017, *MNRAS*, 464, 1077
- Wuyts S., Cox T. J., Hayward C. C., Franx M., Hernquist L., Hopkins P. F., Jonsson P., van Dokkum P. G., 2010, *ApJ*, 722, 1666
- Zavala J. et al., 2016, *MNRAS*, 460, 4466
- Zhu L. et al., 2018, *MNRAS*, 473, 3000
- Zolotov A. et al., 2015, *MNRAS*, 450, 2327

APPENDIX A: ROBUSTNESS TO RESOLUTION

As with any numerical work, it is important to establish that our results are not driven by the resolution of the simulations, which we quantify here by the initial baryonic particle mass $m_{\text{gas},i}$. As we demonstrate here, the morphological parameters of a single galaxy are relatively stable to changes in the resolution, indicating that the morphology is driven by fundamental properties of either the galaxy or halo, not the resolution at which that galaxy is simulated.

The left-hand panel of Fig. A1 plots R_{90}^* and f_{disc}^* explicitly as a function of the resolution of the simulation for several of our galaxies that have been simulated at a variety of resolutions. Lines connect runs of the same galaxy at different resolutions; the runs analysed in the main text are highlighted in orange. Though there are changes with resolution (in particular, galaxies typically tend to be marginally more radially extended and discier at higher resolution), the relative ordering of the simulations stays generally constant and the morphological parameters are generally resolved. Moreover, our results indicate that the FIRE-2 physics can yield roughly flat stellar rotation curves even with initial gas particle masses $m_{i,\text{gas}} = 57,000 M_{\odot}$ (Robin).

The right-hand panel of Fig. A1 plots two of the galaxy properties that we find to correlate with morphology, the amount of gas in the galaxy at $z = 0$ and the spin of the gas within R_{vir} at the half-mass radius of the galaxy.¹⁸ As in the left-hand panel, the majority of the galaxies have properties that are generally stable to resolution, suggesting that the correlations we identify above are robust to resolution.

The largest outliers from these trends are Juliet and Romeo. At the resolution, we analyse here, Juliet experiences an extended prograde encounter with a gas-rich satellite that both torques up the existing disc and deposits substantial fuel for additional discy star formation. Though analysis is still ongoing, preliminary investigations of the high-resolution version of this simulation suggest that the merger is not as well aligned, in line with the trends that we discuss above. Similarly, Romeo experiences a minor merger at $z \sim 0.6$; this merger is again less well aligned in the high-resolution version as the run we analyse here. In both cases, moreover, the morphological measures trend in the same direction as the galaxy properties that correlate with them, further solidifying our conclusions. We also plot an incomplete run of m12q from $z \sim 1.5$ as an open point; because the disc that m12q does build (Fig. 12) does not appear until $z \sim 1$ (after which it is quickly destroyed), the

¹⁸We recalculate a_*^{50} and use the spin factor at each resolution.

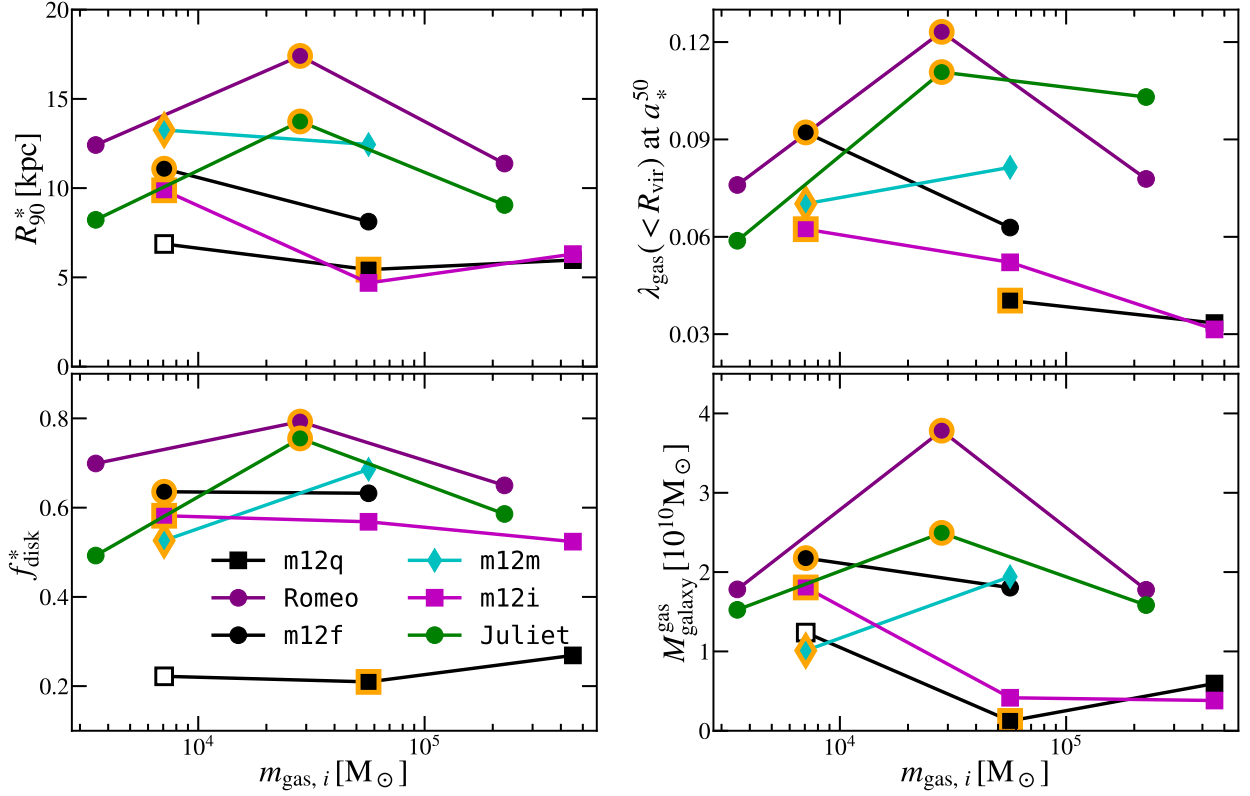


Figure A1. Morphological parameters (left) and properties that we find to correlate with morphology (right) for several of the galaxies as a function of the numerical resolution of the simulation, quantified here by the initial gas particle mass. Though the exact values vary somewhat as a function of resolution, the relative morphologies of the galaxies remain rather consistent; any variations are relatively small (bulgy galaxies remain bulgy, and discy galaxies remain discy), and would not change our conclusions. Moreover, the properties that correlate with morphology in the main body typically trend in the same direction as the morphological measures themselves. The open point of m12q is taken from an incomplete run at $z \sim 1.5$ and is primarily shown for illustrative purposes. The orange-rimmed points indicate the runs analysed in the main body. The higher resolution Romeo & Juliet finished, while the manuscript was in the late stages of preparation, and a full analysis (particularly as a function of time) is still ongoing.

higher resolution version of this galaxy is remarkably similar to the fiducial version, even at this time.

Therefore, we assert that the relative morphologies of several systems may be fairly compared, even if the exact values vary slightly as a function of resolution. That is, there are fundamental, underlying properties of a given host that determine the morphology of that galaxy. We demonstrated above and in the right-hand panel of Fig. A1 that these properties are most strongly related to the formation histories of galaxies and their spin at high redshift.

APPENDIX B: ROTATION CURVES

Fig. B1 plots the circular velocity curves of our galaxies, defined as $\sqrt{GM(<r)}/r$. Generally speaking, galaxies with higher kinematic disc fractions also have flatter, less centrally peaked rotation curves. The exceptions are m12z, the least massive galaxy in our sample, and m12m, which recently underwent a bar-buckling event as noted in the main text.

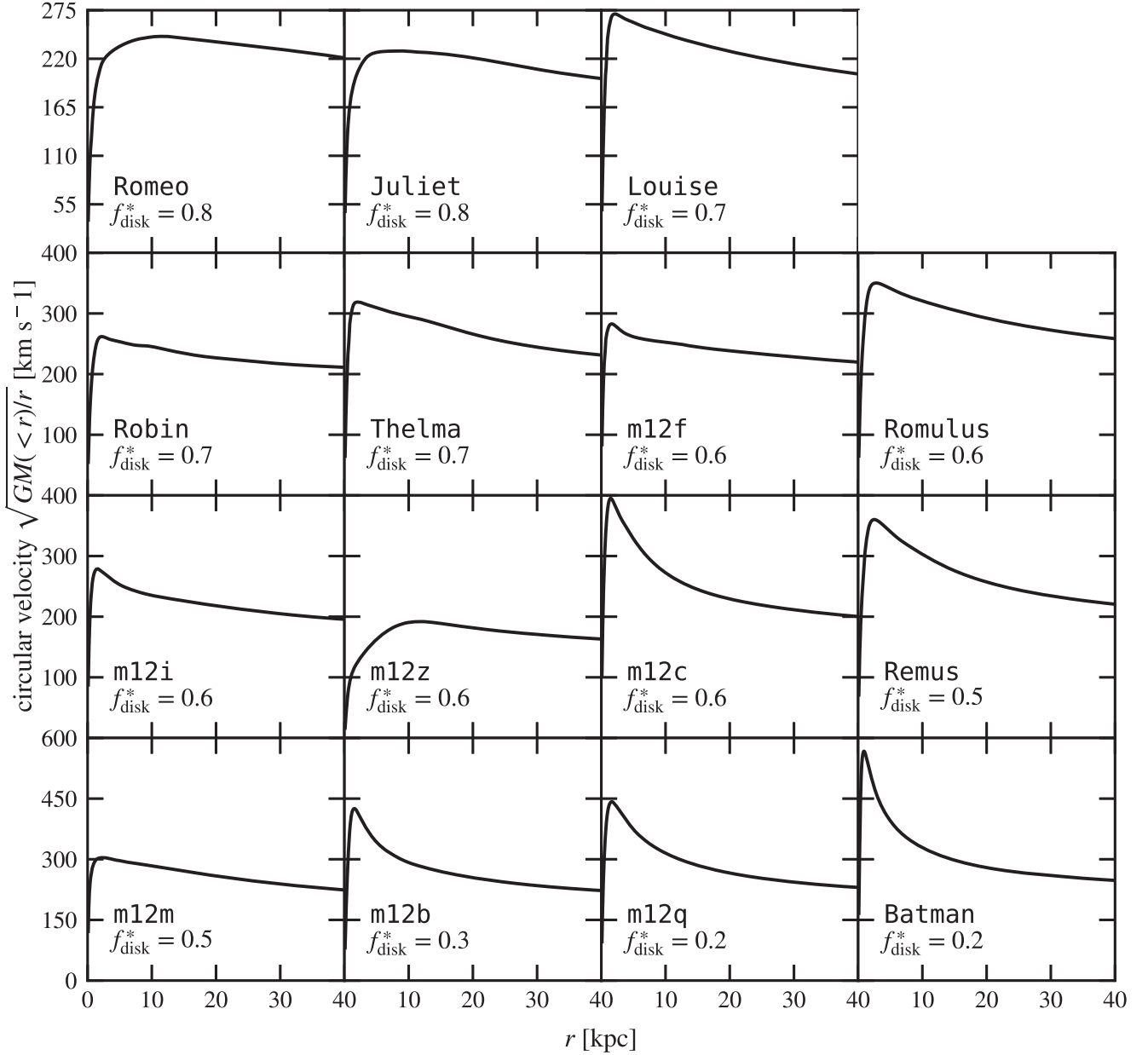


Figure B1. The circular velocity curves of our galaxies, again sorted by decreasing f_{disk}^* . The bulge-dominated galaxies are also generally the most concentrated, and therefore tend to be more centrally peaked. The disciest galaxies, however, have smoothly rising rotation curves and peak at $\lesssim 250 \text{ km s}^{-1}$ at 5–10 kpc, as does m12z, our lowest mass host. Note that the scales of the y-axes vary from row to row to capture the behaviour of the more centrally concentrated galaxies.

APPENDIX C: GROWTH HISTORIES

Fig. 7 plots the growth of the halo mass, total gas mass, cold gas mass in the halo, stellar mass, and gas fractions for three representative galaxies, Juliet, m12i, and Batman. For completeness, we plot the entirety of our sample in Fig. C1. The trends that we identify

regarding the relative amount of star-forming gas using the three representative galaxies in Fig. 7 are robust – at higher disc fractions, the galaxies almost uniformly reach their peak $M_{\text{cold}}^{\text{gas}}$ at later times and typically maintain that level of star-forming gas for several gigayears.

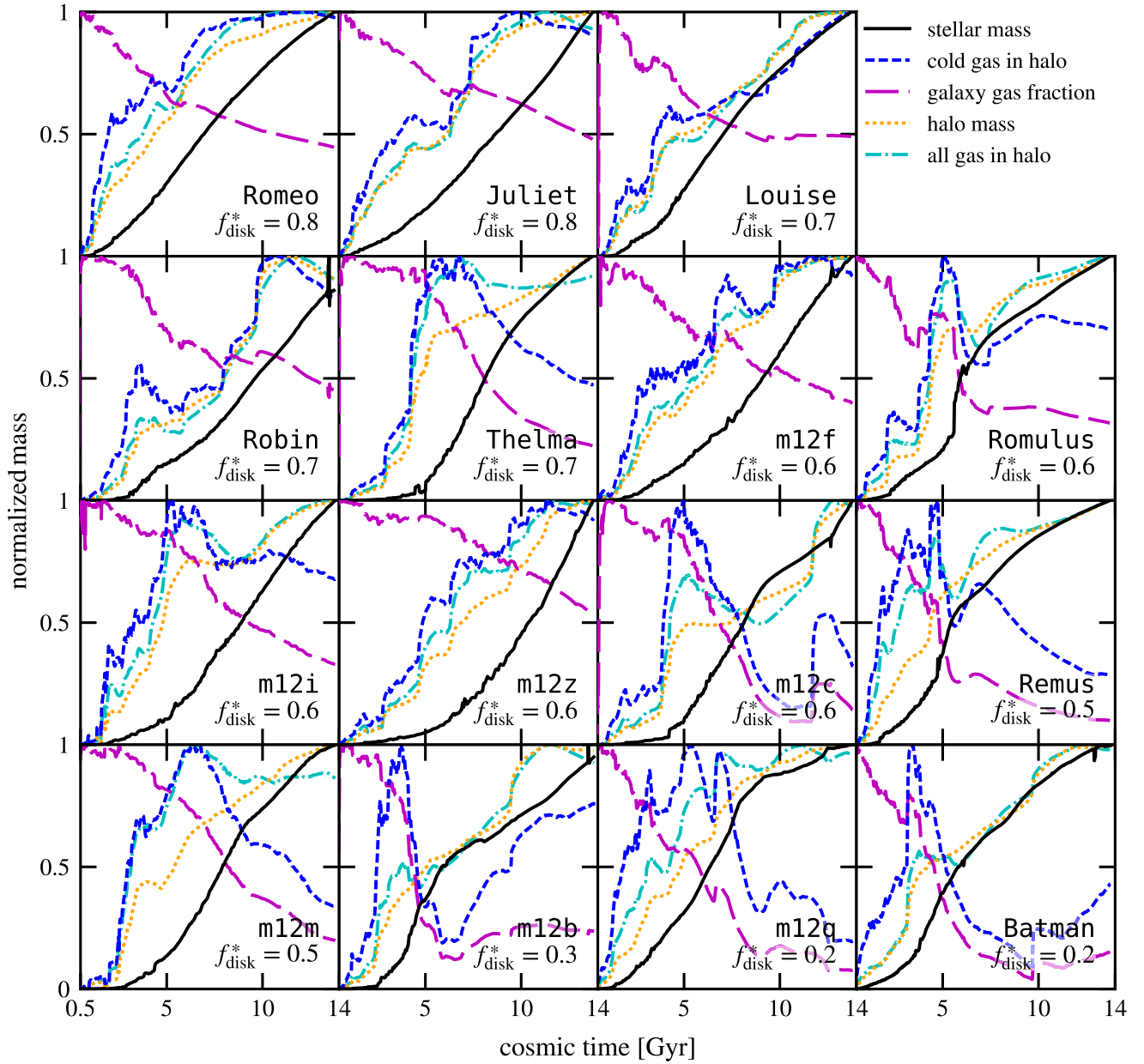


Figure C1. Identical to Fig. 7, but showing our full sample.

This paper has been typeset from a \LaTeX file prepared by the author.